



HAL
open science

Nonlinear nanomechanical resonators approaching the quantum ground state

C. Samanta, S. de Bonis, C. Møller, R. Tormo-Queralt, W. Yang, C. Urgell, B. Stamenic, B. Thibeault, Y. Jin, D. Czaplewski, et al.

► **To cite this version:**

C. Samanta, S. de Bonis, C. Møller, R. Tormo-Queralt, W. Yang, et al.. Nonlinear nanomechanical resonators approaching the quantum ground state. *Nature Physics*, 2023, 10.1038/s41567-023-02065-9. hal-04148748

HAL Id: hal-04148748

<https://hal.science/hal-04148748>

Submitted on 3 Jul 2023

HAL is a multi-disciplinary open access archive for the deposit and dissemination of scientific research documents, whether they are published or not. The documents may come from teaching and research institutions in France or abroad, or from public or private research centers.

L'archive ouverte pluridisciplinaire **HAL**, est destinée au dépôt et à la diffusion de documents scientifiques de niveau recherche, publiés ou non, émanant des établissements d'enseignement et de recherche français ou étrangers, des laboratoires publics ou privés.

Nonlinear nanomechanical resonators approaching the quantum ground state

C. Samanta,¹ S. L. De Bonis,¹ C. B. Møller,¹ R. Tormo-Queralt,¹ W. Yang,¹ C. Urgell,¹ B. Stamenic,² B. Thibeault,² Y. Jin,³ D. A. Czaplewski,⁴ F. Pistolesi,⁵ and A. Bachtold¹

*¹ICFO - Institut De Ciències Fotoniques,
The Barcelona Institute of Science and Technology,
08860 Castelldefels (Barcelona), Spain*

²UCSB Nanofabrication Facility, ECE Department, Santa Barbara, CA 93106, USA

³C2N, CNRS, Université Paris-Saclay, 91120 Palaiseau, France

⁴Center for Nanoscale Materials, Argonne National Laboratory, Argonne, IL 60439, USA

*⁵Université de Bordeaux, CNRS, LOMA,
UMR 5798, F-33400 Talence, France*

Abstract

An open question in mechanics is whether mechanical resonators can be made nonlinear with vibrations approaching the quantum ground state. This requires engineering a mechanical nonlinearity far beyond what has been realized thus far. Here we discovered a mechanism to boost the Duffing nonlinearity by coupling the vibrations of a nanotube resonator to single-electron tunneling and by operating the system in the ultrastrong coupling regime. Remarkably, thermal vibrations become highly nonlinear when lowering the temperature. The average vibration amplitude at the lowest temperature is 13 times the zero-point motion, with approximately 42% of the thermal energy stored in the anharmonic part of the potential. Our work paves the way for realizing mechanical ‘Schrödinger cat’ states [1], mechanical qubits [2, 3], and quantum simulators emulating the electron-phonon coupling [4].

Mechanical resonators are perfect linear systems in experiments carried out in the quantum regime. Such devices enable quantum squeezing of the mechanical motion [5–7], quantum backaction evading measurements [8–10], and entanglement between mechanical resonators [11, 12]. Achieving nonlinear vibrations in resonators approaching the quantum ground state would offer novel prospects for the quantum control of their motion. These include the development of mechanical qubits [2, 3] and mechanical cat states [1]. However, creating the strong nonlinearities required for this endeavour has been out of reach in all the mechanical systems explored thus far.

Mechanical resonators become nonlinear at large vibration amplitude x , when the Duffing (or Kerr) nonlinear term of the restoring force is sizable. Specifically, the restoring force reads $F = -m\omega_m^2 x - \gamma x^3$ with m the mechanical eigenmode mass, ω_m the resonance frequency, and γ the Duffing constant. The Duffing constant is usually small but can be engineered using a force field gradient or a two-level system [13]. Although mechanical systems have been operated in large field gradients [14, 15] and strongly coupled to two-level systems [16–23], it has not been possible to create sizeable Duffing nonlinearities for vibrations approaching the quantum ground state.

We demonstrate a new mechanism to boost the vibration nonlinearity by coupling the mechanical resonator to single-electron tunneling (SET) in a quantum dot (Figs. 1a,b). The latter is operated as a degenerate two-level system fluctuating between two states with N and $N + 1$ electrons. The capacitive coupling to the mechanical mode is described by the Hamiltonian $H = -\hbar g n x / x_{zp}$, where g is the electromechanical coupling, $n = 0, 1$ the additional electron number in the quantum dot, and x_{zp} is the vibration zero-point motion. In the adiabatic limit, when the electron fluctuation rate is faster than the bare mechanical frequency ($\Gamma_e > \omega_m^o$), the fluctuations result in the nonlinear restoring force given by

$$F_{\text{eff}} = - \left[m\omega_m^o{}^2 - \frac{1}{4x_{zp}^2} \frac{(\hbar g)^2}{k_B T} \right] x - \frac{1}{48x_{zp}^4} \frac{(\hbar g)^4}{(k_B T)^3} x^3 \quad (1)$$

when the electronic two-level system is degenerate (Fig. 1b; Sup. Info. Sec. I.D). A striking aspect of the nonlinearity is its temperature dependence, since the nonlinear Duffing constant significantly increases when reducing temperature. The vibration potential can even become purely quartic in displacement, since the linear part of the restoring force vanishes [24] at low temperature when $2k_B T = \hbar g^2 / \omega_m^o$. This can be realized for mechanical systems not in their motional ground state ($k_B T > \hbar \omega_m^o$) by operating the system in the ultrastrong

coupling regime when $g > \sqrt{2}\omega_m^o$. Equation 1 also indicates that the measurement of a large decrease of ω_m at low temperature is a direct indication of a strong nonlinearity. A large number of experiments have been carried out where mechanical vibrations are coupled to SET [25–33], but the decrease of ω_m has always been modest.

Carbon nanotube electromechanical resonators (Fig. 1a) are uniquely suited for demonstrating a strong vibration nonlinearity. Its ultra-low mass gives rise to a large coupling g , which is directly proportional to $x_{zp} = \sqrt{\hbar/2\omega_m^o m}$. Moreover, high-quality quantum dots can be defined along the nanotube by two p-n tunnel junctions that are controlled by electrostatic means. Figure 1c shows a conductance trace featuring regular peaks associated with SET through the system.

A large dip in ω_m is observed when setting the system on a conductance peak (Figs. 2a,b) where the electronic two-level system is degenerate. This is consistent with the vibration potential becoming strongly anharmonic. The decrease of ω_m is enhanced at lower temperatures (Fig. 2c), indicating that the high temperature harmonic potential smoothly evolves into an increasingly anharmonic potential. These data are well reproduced by the universal function predicted for ω_m , which depends only on the ratio $\epsilon_P/k_B T$ (Sup. Info. Eq. 44); here $\epsilon_P = 2\hbar g^2/\omega_m^o$. Similar decrease in ω_m was observed in two other devices (Sup. Info. Sec. II.H).

These measurements reveal that the system is deep in the ultrastrong coupling regime. The universal temperature dependence of ω_m enables us to quantify g with accuracy. The largest coupling obtained from measurements at different conductance peaks is $g/2\pi = 500 \pm 36$ MHz (black dots in Fig. 3a), corresponding to $g/\omega_m^o = 16.5 \pm 1.2$. The coupling is consistent with the estimation $g/2\pi = 547 \pm 185$ MHz obtained from independent measurements where the coupling is determined from the capacitive force associated with one electron added onto the quantum dot (purple line in Fig. 3a). The large uncertainty of this second estimation is related to the measurement of the eigenmode mass that enters the zero-point motion expression. Figures 3a-c show that the device is operated in the ultrastrong coupling regime $g > \omega_m^o$ and the adiabatic limit $\Gamma_e > \omega_m^o$, which are necessary conditions to realize strong vibration anharmonicity.

We now turn our attention to the driven nonlinear resonant response of the mechanical mode (Figs. 4a,b). The spectral peak is asymmetric for vibration amplitudes as low as $x \simeq 40 \times x_{zp}$. We do not observe the usual hysteresis in the nonlinear response when

the driving frequency is swept back and forth. Moreover, the nonlinear resonator has a decreasing responsivity for an increasing drive (Fig. 4c). These data agree with a model that takes into account the strong nonlinearity and thermal fluctuations; see the red lines in Figs. 4a,c. The lack of hysteresis is explained by the low amplitude of driven vibrations compared to the thermal displacement amplitude, an unusual regime for driven nonlinear response measurements [13]. The behaviour of the responsivity arises from the thermal fluctuations that modify the spectral response of the driven nonlinear resonator [13]. By comparing the model to the whole measured set of spectra spanning the linear-nonlinear crossover (Figs. 4a,c), we determine the coupling $g/2\pi = 646 \pm 217$ MHz. We obtain $g/2\pi = 757 \pm 197$ MHz from the quadratic dependence of the resonant frequency on the driven vibrational amplitude for Duffing resonators (Fig. 4b), which remains approximately valid in the presence of thermal fluctuations provided that the driven vibration amplitude is sufficiently small. These two values of g are consistent with the two first estimates.

The vibrations become strongly nonlinear at low temperature for vibrations approaching the quantum ground state. Figure 4d shows the fraction of the thermal energy stored in the nonlinear part of the vibration potential $\mathcal{U}_{\text{NL}} = [\langle U_{\text{eff}}(x) \rangle - m\omega_m^2 \langle x^2 \rangle / 2] / \langle U_{\text{eff}}(x) \rangle$ where $U_{\text{eff}}(x)$ is the total effective vibration potential created by the coupling. The fraction is directly estimated from the measured decrease of ω_m using the theory predictions of the coupled system (Sup. Info. Sec. I.F). The effect of the nonlinearity on the vibrations becomes increasingly important as the temperature is decreased, since a larger fraction of the thermal energy is stored in the nonlinear part of the potential (Fig. 4d). The fraction \mathcal{U}_{NL} becomes approximately 42% at the lowest measured temperature where the average amplitude of thermal vibrations is $x_{\text{th}} \simeq 13 \times x_{\text{zp}}$. Having the nonlinear part of the restoring force comparable to its linear part is extreme for mechanical resonators, especially when considering that the thermal vibration amplitude is so close to the zero-point motion.

We have demonstrated a mechanism to create a strong mechanical nonlinearity by coupling a mechanical resonator and a two-level system in the ultrastrong coupling regime. Mechanical resonators endowed with a sizeable nonlinearity in the quantum regime enable numerous applications. Novel qubits may be engineered where the information is stored in the mechanical vibrations; such mechanical qubits are expected to inherit the long coherence time of the mechanical vibrations and may be used for manipulating quantum information [2, 3]. Mechanical ‘Schrodinger cat’ states — non-classical superpositions of

mechanical coherent states — can also be formed [1] with enhanced quantum sensing capabilities in the detection of force and mass. In practice, such systems may be realized by coupling the mechanical vibrations to double-quantum dots [29]. This approach preserves both the strong mechanical nonlinearities measured in this work [3] and high mechanical quality factors [30, 34]. Coupling mechanical vibrations to yet more quantum dots in a linear array may realize an analogue quantum simulator of small-size quantum materials [4]. Such a simulator could explore the rich physics of strongly correlated systems where the electron-electron repulsion is competing with the electron-phonon interaction.

-
- [1] G. Kirchmair, B. Vlastakis, Z. Leghtas, S. E. Nigg, H. Paik, E. Ginossar, M. Mirrahimi, L. Frunzio, S. M. Girvin, and R. J. Schoelkopf, *Nature* **495**, 205 (2013), ISSN 1476-4687.
 - [2] S. Rips and M. J. Hartmann, *Phys. Rev. Lett.* **110**, 120503 (2013), URL <https://link.aps.org/doi/10.1103/PhysRevLett.110.120503>.
 - [3] F. Pistolesi, A. N. Cleland, and A. Bachtold, *PRX* **11**, 031027 (2021), URL <https://link.aps.org/doi/10.1103/PhysRevX.11.031027>.
 - [4] U. Bhattacharya, T. Grass, A. Bachtold, M. Lewenstein, and F. Pistolesi, *Nano Lett.* **21**, 9661 (2021), ISSN 1530-6984, URL <https://doi.org/10.1021/acs.nanolett.1c03457>.
 - [5] J.-M. Pirkkalainen, E. Damskäg, M. Brandt, F. Massel, and M. A. Sillanpää, *Phys Rev Lett* **115**, 243601 (2015).
 - [6] F. Lecocq, J. B. Clark, R. W. Simmonds, J. Aumentado, and J. D. Teufel, *Phys. Rev. X* **5**, 041037 (2015).
 - [7] E. E. Wollman, C. U. Lei, A. J. Weinstein, J. Suh, A. Kronwald, F. Marquardt, A. A. Clerk, and K. C. Schwab, *Science* **349**, 952 (2015).
 - [8] J. Suh, A. J. Weinstein, C. U. Lei, E. E. Wollman, S. K. Steinke, P. Meystre, A. A. Clerk, and K. C. Schwab, *Science* **344**, 1262 (2014), URL <http://science.sciencemag.org/content/344/6189/1262.abstract>.
 - [9] C. F. Ockeloen-Korppi, E. Damskäg, J.-M. Pirkkalainen, A. A. Clerk, M. J. Woolley, and M. A. Sillanpää, *PRL* **117**, 140401 (2016), URL <https://link.aps.org/doi/10.1103/PhysRevLett.117.140401>.
 - [10] C. B. Møller, R. A. Thomas, G. Vasilakis, E. Zeuthen, Y. Tsaturyan, M. Balabas, K. Jensen,

- A. Schliesser, K. Hammerer, and E. S. Polzik, *Nature* **547**, 191 (2017), ISSN 1476-4687, URL <https://doi.org/10.1038/nature22980>.
- [11] S. Kotler, G. A. Peterson, E. Shojaee, F. Lecocq, K. Cicak, A. Kwiatkowski, S. Geller, S. Glancy, E. Knill, R. W. Simmonds, et al., *Science* **372**, 622 (2021), URL <https://doi.org/10.1126/science.abf2998>.
- [12] E. A. Wollack, A. Y. Cleland, R. G. Gruenke, Z. Wang, P. Arrangoiz-Arriola, and A. H. Safavi-Naeini, *Nature* **604**, 463 (2022), ISSN 1476-4687, URL <https://doi.org/10.1038/s41586-022-04500-y>.
- [13] A. Bachtold, J. Moser, and M. Dykman, *Review Modern Physics* (in press) preprint arXiv:2202.01819 (2022).
- [14] A. Gloppe, P. Verlot, E. Dupont-Ferrier, A. Siria, P. Poncharal, G. Bachelier, P. Vincent, and O. Arcizet, *Nature Nanotechnology* **9**, 920 (2014), ISSN 1748-3395, URL <https://doi.org/10.1038/nnano.2014.189>.
- [15] Q. P. Unterreithmeier, E. M. Weig, and J. P. Kotthaus, *Nature* **458**, 1001 (2009), ISSN 1476-4687, URL <https://doi.org/10.1038/nature07932>.
- [16] J. Kettler, N. Vaish, L. M. de Lépinay, B. Besga, P.-L. de Assis, O. Bourgeois, A. Auffèves, M. Richard, J. Claudon, J.-M. Gérard, et al., *Nature Nanotechnology* **16**, 283 (2021), ISSN 1748-3395, URL <https://doi.org/10.1038/s41565-020-00814-y>.
- [17] A. D. O'Connell, M. Hofheinz, M. Ansmann, R. C. Bialczak, M. Lenander, E. Lucero, M. Neeley, D. Sank, H. Wang, M. Weides, et al., *Nature* **464**, 697 (2010).
- [18] K. J. Satzinger, Y. P. Zhong, H.-S. Chang, G. A. Peairs, A. Bienfait, M.-H. Chou, A. Y. Cleland, C. R. Conner, E. Dumur, J. Grebel, et al., *Nature* **563**, 661 (2018).
- [19] Y. Chu, P. Kharel, T. Yoon, L. Frunzio, P. T. Rakich, and R. J. Schoelkopf, *Nature* **563**, 666 (2018).
- [20] P. Arrangoiz-Arriola, E. A. Wollack, Z. Wang, M. Pechal, W. Jiang, T. P. McKenna, J. D. Witmer, R. V. Laer, and A. H. Safavi-Naeini, *Nature* **571**, 537 (2019).
- [21] M. D. LaHaye, J. Suh, P. M. Echternach, K. C. Schwab, and M. L. Roukes, *Nature* **459**, 960 (2009).
- [22] J.-M. Pirkkalainen, S. U. Cho, J. Li, G. S. Paraoanu, P. J. Hakonen, and M. A. Sillanpää, *Nature* **494**, 211 (2013), ISSN 1476-4687, URL <https://doi.org/10.1038/nature11821>.
- [23] X. Ma, J. J. Viennot, S. Kotler, J. D. Teufel, and K. W. Lehnert, *Nature Physics* **17**, 322

- (2021), ISSN 1745-2481, URL <https://doi.org/10.1038/s41567-020-01102-1>.
- [24] G. Micchi, R. Avriller, and F. Pistolesi, Phys. Rev. Lett. **115**, 206802 (2015), URL <https://link.aps.org/doi/10.1103/PhysRevLett.115.206802>.
- [25] R. G. Knobel and A. N. Cleland, Nature **424**, 291 (2003), URL <http://dx.doi.org/10.1038/nature01773>.
- [26] B. Lassagne, Y. Tarakanov, J. Kinaret, D. Garcia-Sanchez, and A. Bachtold, Science **325**, 1107 (2009).
- [27] G. A. Steele, A. K. Hüttel, B. Witkamp, M. Poot, H. B. Meerwaldt, L. P. Kouwenhoven, and H. S. J. van der Zant, Science **325**, 1103 (2009).
- [28] Y. Okazaki, I. Mahboob, K. Onomitsu, S. Sasaki, and H. Yamaguchi, Nature Communications **7**, 11132 (2016), ISSN 2041-1723, URL <https://doi.org/10.1038/ncomms11132>.
- [29] I. Khivrich, A. A. Clerk, and S. Ilani, Nature Nanotechnology **14**, 161 (2019), ISSN 1748-3395, URL <https://doi.org/10.1038/s41565-018-0341-6>.
- [30] C. Urgell, W. Yang, S. L. De Bonis, C. Samanta, M. J. Esplandiu, Q. Dong, Y. Jin, and A. Bachtold, Nat. Phys. **16**, 32 (2020).
- [31] Y. Wen, N. Ares, F. J. Schupp, T. Pei, G. A. D. Briggs, and E. A. Laird, Nat. Phys. **16**, 75 (2020).
- [32] S. Blien, P. Steger, N. Hittner, R. Graaf, and A. K. Hüttel, Nature Communications **11**, 1636 (2020), ISSN 2041-1723, URL <https://doi.org/10.1038/s41467-020-15433-3>.
- [33] F. Vigneau, J. Monsel, J. Tabanera, L. Bresque, F. Fedele, G. D. Briggs, J. Anders, J. M. Parrondo, A. Auffèves, and N. Ares, preprint arXiv:2103.15219 (2021).
- [34] J. Gardner, S. D. Bennett, and A. A. Clerk, Phys. Rev. B **84**, 205316 (2011), URL <https://link.aps.org/doi/10.1103/PhysRevB.84.205316>.

Acknowledgements: We acknowledge support from ERC Advanced Grant No. 692876, Marie Skłodowska-Curie grant agreement No. 101023289, MICINN Grant No. RTI2018-097953-B-I00, AGAUR (Grant No. 2017SGR1664), the Quanterra grant (PCI2022-132951), the Fondo Europeo de Desarrollo, the Spanish Ministry of Economy and Competitiveness through Quantum CCAA and CEX2019-000910-S [MCIN/AEI/10.13039/501100011033],

MCIN with funding from European Union NextGenerationEU(PRTR-C17.I1), Fundacio Cellex, Fundacio Mir-Puig, Generalitat de Catalunya through CERCA. Work performed at the Center for Nanoscale Materials, a U.S. Department of Energy Office of Science User Facility, was supported by the U.S. DOE, Office of Basic Energy Sciences, under Contract No. DE-AC02-06CH11357.

Author contributions: CS, SLDB and DAC fabricated the devices with contributions from BS and BT. CS and SLDB carried out the measurements with support from CBM, RTQ, WY and CU. YB provided the amplifier used in the measurements. FP developed the theory. CS, SLDB, FP and AB analyzed the data. CS, CBM, DAC, FP and AB wrote the manuscript with inputs from the other authors. AB supervised the work.

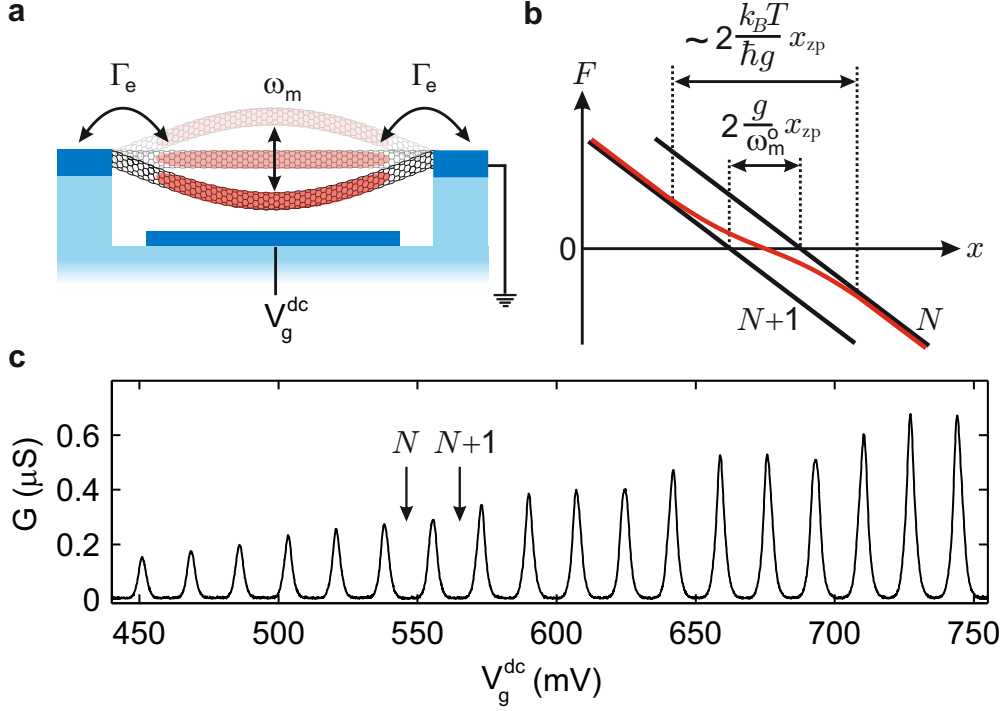


Fig. 1: SET-based nonlinearity. (a) Schematics of the nanotube vibrating at ω_m . A quantum dot highlighted in red is formed along the suspended nanotube; the total electron tunnel rate to the two leads is Γ_e . The vibrations are coupled to the electrons in the quantum dot via the capacitive coupling between the nanotube and the gate electrode. (b) Origin of the SET-based nonlinearity. The two linear force-displacement curves shown in black correspond to the dot filled with either N or $N + 1$ electrons; the slope is given by the spring constant $m\omega_m^0{}^2$ and the two curves are separated by $\Delta x = 2(g/\omega_m^0)x_{zp}$ caused by the force created by one electron tunnelling onto the quantum dot. The force felt by the vibrations is an average of the two black forces weighted by the Fermi-Dirac distribution when $\Gamma_e > \omega_m^0$. The resulting force in red is nonlinear for vibration displacements smaller than $\sim \frac{k_B T}{\hbar g} x_{zp}$; the reduced slope at zero vibration displacement indicates the decrease of ω_m . (c) Gate voltage dependence of the conductance G of device I at $T=6$ K. The average dot occupation increases by about one electron over the gate voltage range where a G peak is observed. A voltage smaller than $k_B T/e$ is applied to measure G .

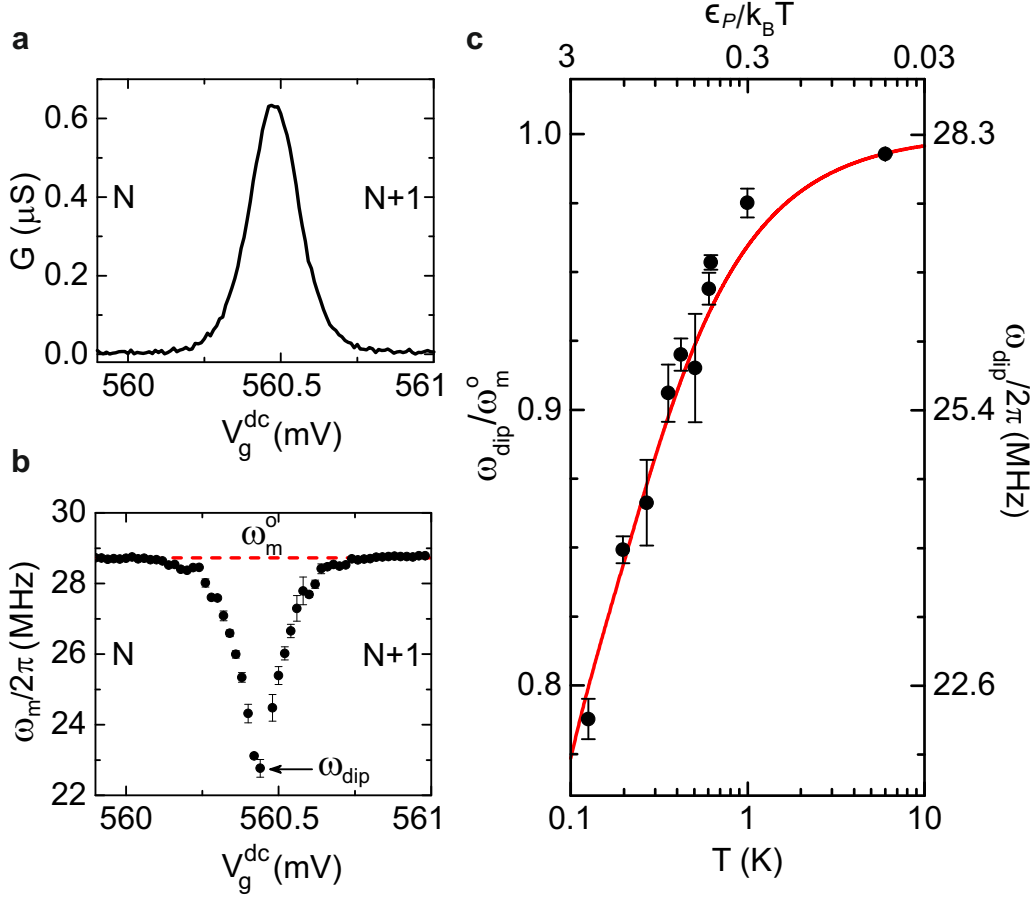


Fig. 2: Enhanced mechanical vibration nonlinearity at low temperature. (a,b) Conductance and mechanical resonance frequency as a function of gate voltage V_g^{dc} at 300 mK. By counting the number of observed conductance peaks from the nanotube energy gap, we estimate $N = 22$. The red dashed line indicates ω_m^o . (c) Temperature dependence of the resonance frequency. The red solid line is the predicted universal function. The $\omega_{\text{dip}}/\omega_m^o$ reduction is expected to be about 0.75 when the potential is quartic; in this case, while the linear part of F_{eff} is zero, the nonlinear part of F_{eff} combined with thermal vibrations significantly renormalizes ω_m .

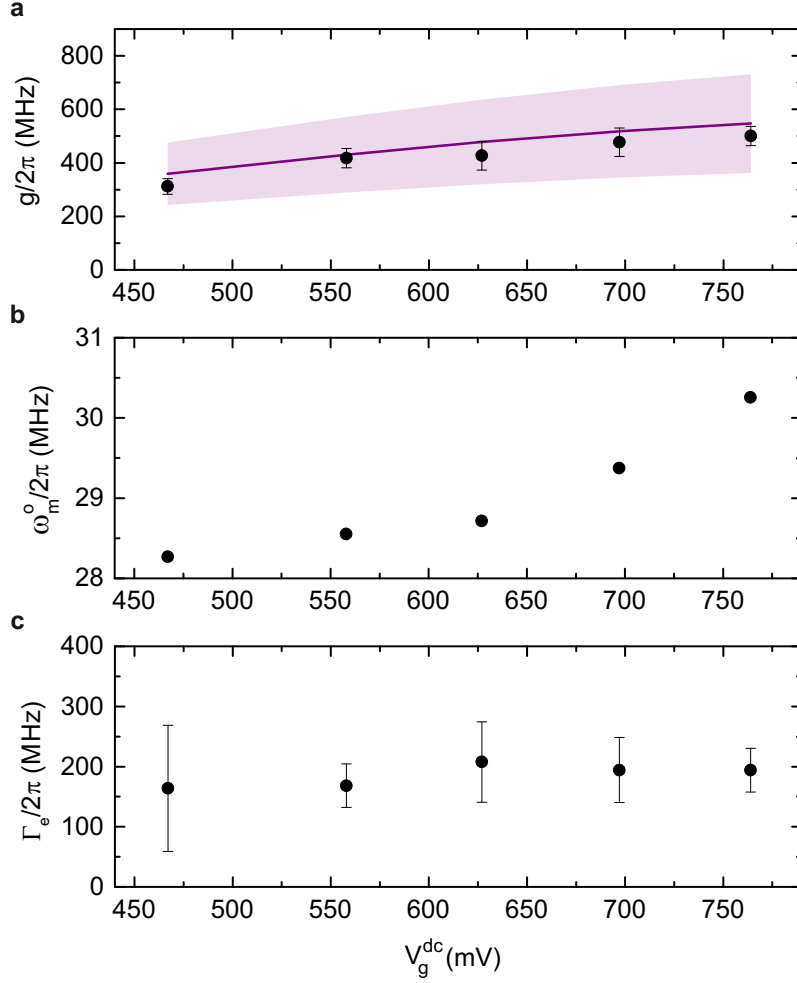


Fig. 3: Electromechanical resonator in the ultrastrong coupling regime. (a) Coupling g as a function of V_g^{dc} . The black data points are obtained from the measured temperature dependence of ω_m . The purple line is estimated from $g = e(C'_g/C_\Sigma)V_g^{\text{dc}}/\sqrt{2m\hbar\omega_m^o}$ where m is quantified from driven spectral response measurements and where the spatial derivative of the dot-gate capacitance C'_g and the V_g^{dc} -dependent total capacitance C_Σ of the quantum dot are obtained from electron transport measurements. The uncertainty in this second estimation of g is shown by the purple shaded area. (b,c) Bare mechanical resonance frequency ω_m^o and electron tunnel rate Γ_e as a function of V_g^{dc} . The ω_m^o variation is due to the electrostatically-induced stress in the nanotube. We quantify Γ_e from the temperature dependence of the resonance width $\Delta\omega$ in the spectral response measurements.

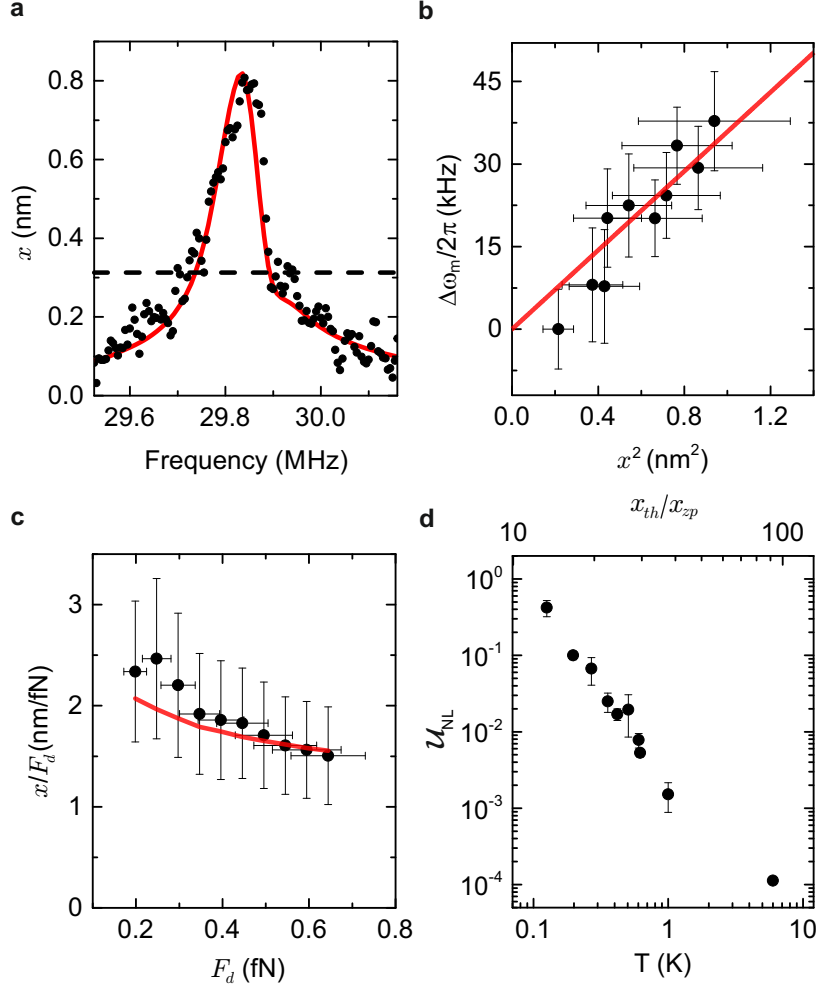


Fig. 4: Nonlinear mechanical vibrations at $V_g^{\text{dc}} = 757.2$ mV. (a) Nonlinear resonant response to the driving force at 6 K. The dashed black line corresponds to $x = 40 \times x_{\text{zp}}$. The red line is the simultaneous fit of 10 spectra at different drives, which span the linear-nonlinear crossover, to the theoretical prediction (Sup. Info. Sec. I.H). The response gets difficult to measure at lower T , since the vibration dissipation is enhanced and the drive is set by the oscillating gate voltage that has to be a few times smaller than the V_g^{dc} width of the G peak to avoid electrical nonlinearities. (b) Resonant frequency shift versus the driven vibration amplitude at 6 K. The red line is a linear fit to the data. The driven vibration amplitude is set smaller or comparable to the averaged amplitude of the thermal vibrations x_{th} . (c) Responsivity x/F_d of the mechanical mode at 6 K, where F_d is the driven force amplitude. The red line is the fit to the theoretical prediction (Sup. Info. Sec. I.H). (d) Ratio \mathcal{U}_{NL} between the thermal vibration energy stored in the nonlinear part of the potential and that in the total vibration potential.

Supplementary Information

Nonlinear nanomechanical resonators approaching the quantum ground state

C. Samanta,¹ S. L. De Bonis,¹ C. B. Møller,¹ R. Tormo Queralt,¹ W. Yang,¹ C. Urgell,¹
B. Stamenic,² B. Thibeault,² Y. Jin,³ D. A. Czaplewski,⁴ F. Pistolesi,⁵ and A. Bachtold¹

¹*ICFO - Institut De Ciències Fotoniques, The Barcelona Institute of
Science and Technology, 08860 Castelldefels (Barcelona), Spain*

²*UCSB Nanofabrication Facility, ECE Department, Santa Barbara, CA 93106, USA*

³*C2N, CNRS, Université Paris-Saclay, Palaiseau, France*

⁴*Center for Nanoscale Materials, Argonne National Laboratory, Argonne, IL, 60439, USA*

⁵*Université de Bordeaux, CNRS, LOMA, UMR 5798, F-33400 Talence, France*

(Dated: November 15, 2022)

Contents

| | |
|---|-----------|
| I. Theoretical description | 1 |
| A. Central results | 1 |
| B. Electronic transport | 2 |
| C. Back-action on the oscillator | 3 |
| D. Effective potential | 4 |
| E. Fluctuation spectrum and softening of the mechanical mode | 5 |
| F. Coefficients of a series expansion of the potential in the displacement and estimation of the thermal energy stored in the non-harmonic part of the potential | 6 |
| G. Nonlinear Duffing response in presence of thermal fluctuations | 7 |
| H. Procedure used to fit the nonlinear Duffing response | 8 |
| II. Experimental Section | 9 |
| A. Device production | 9 |
| B. Electrical characterization | 9 |
| C. Temperature calibration | 10 |
| D. Detection of mechanical vibrations and estimation of the effective mass | 11 |
| E. Electromechanical coupling and electron tunnel rate | 12 |
| F. Nonlinear spectral response of mechanical vibrations | 13 |
| G. Responsivity of mechanical vibrations | 13 |
| H. Strong anharmonicity in two other devices | 14 |
| I. Estimation of error bars in the figures of the main text | 14 |
| J. Parameters of Device I discussed in the main text | 15 |
| References | 15 |

I. THEORETICAL DESCRIPTION

A. Central results

We first highlight the main theoretical results that emerge from the coupling of a nanomechanical resonator coupled to a quantum dot operated in the incoherent single-electron tunneling regime. When the vibrations are slow with respect to the typical electronic tunneling rate, one finds that the effective force reads:

$$F_{\text{eff}}(x) = -m\omega_m^o{}^2 x + F_e f_F(\epsilon - F_e x), \quad (1)$$

where m is the eigenmode mass, ω_m^o is the bare resonance frequency, $F_e = \hbar g/x_{zp}$ is the variation of the force acting on the mechanical system when the number of electrons in the dot varies by one unit, ϵ is the electron energy level, and f_F is the Fermi-Dirac function. One can define a resonance frequency from the quadratic term of the effective vibration potential obtained by the integration of F_{eff} . It reads $\omega_Q = \omega_m^o(1 - \epsilon_P/4k_B T)^{1/2}$ where $\epsilon_P = 2\hbar g^2/\omega_m^o$ is the polaronic energy, T the temperature, and k_B the Boltzmann constant. Remarkably, the resonance frequency ω_Q associated with the linear restoring force decreases when lowering the temperature and vanishes at $T = 4\epsilon_P/k_B$. The dependence of ω_Q as a function of $\epsilon_P/k_B T$ is shown as a dotted (yellow) line in Fig. S1.

Another striking effect of the coupling and of the suppression of ω_Q is that the nonlinear part of the restoring force becomes dominant at low temperatures. Due to this non-linearity, the period of oscillation becomes strongly dependent on the oscillation amplitude. Thermal fluctuations allow the oscillator to explore different amplitudes, and thus different resonance frequencies: When averaged, these fluctuations lead to an observed resonance frequency that is much higher than ω_Q (see the red line in Fig. S1). In other words, the effect of the non-linearity becomes more important when the vibrations are cooled to low temperature. This is just the opposite of what has been observed in mechanical resonators so far.

Despite the rich physics at work, the temperature dependence of the observed resonance frequency is a universal function of $\epsilon_P/k_B T$ for weak damping. We find

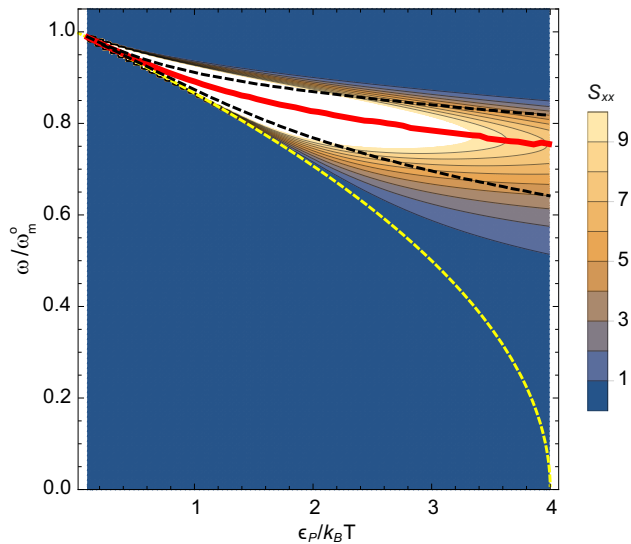


Fig. S1: Contour plot on the plane $\epsilon_P/k_B T$ - ω of the intensity of the spectrum $S_{xx}(\omega)$ in units of $\epsilon_P/m\omega_0^3$. The spectrum is evaluated at a conductance peak; this is the well-known peak arising from single-electron tunneling in quantum dots as the gate voltage is swept. The thick continuous red line indicates the maximum of the spectrum, the dashed black lines indicates the values ω for which the intensity of the spectrum is reduced by a factor of 2 with respect to the maximum. The yellow dotted line is the prediction of Eq. (35) for the value of ω_Q .

this by calculating the displacement fluctuation spectrum $S_{xx}(\omega)$ (shown as a density plot in Fig. S1). It has been shown [1] that $S_{xx}(\omega)$ is proportional to the amplitude response to a weak drive, which is what we measure in this work. The temperature dependence of the measured resonance frequency in Fig. 2c of the main text agrees well with the prediction shown by the full red line in Fig. S1. It is used to extract the value of ϵ_P and, therefore, g . In the remaining part of the section I, we use ω_0 instead of ω_m^o for the bare resonance frequency to make the expressions more compact.

This section provides the basic theoretical description of the problem. It is structured as follows. In Sec. IB we will first recall the standard description of incoherent transport in a single-electron transistor. We then derive in Sec. IC the back-action of the electronic transport on the oscillator, obtaining an expression for the damping coefficient and the quadratic coefficient of the effective potential. In Sec. ID we derive in the equilibrium case the full non-linear effective potential of the oscillator. We obtain ω_Q from the quadratic term of the effective potential. In Sec. IE we derive the displacement fluctuation spectrum $S_{xx}(\omega)$ for the oscillator at equilibrium and discuss its behaviour. In Sec. IF we derive expressions for the first four coefficients in the expansion in the displacement x of the effective potential and the average of the

full non-linearity. In Sec. IG we recall the main steps of the derivation of the Fokker-Planck equation for the oscillator quadratures in a Duffing description of the response to a drive. We then describe how we have used its numerical solution to fit the observed nonlinear spectra (Sec.IH).

B. Electronic transport

Electronic transport measurements in the device are described by incoherent tunnelling in the Coulomb blockade regime. This corresponds to the condition $\hbar\Gamma_e \ll k_B T \ll \Delta E \ll E_C$, where Γ_e is the tunneling rate of the electrons to the quantum dot, $E_C = e^2/C_\Sigma$ is the Coulomb energy (C_Σ the total capacitance of the dot, ΔE the electronic level spacing, e the electron charge). For a description of transport in this regime see for instance Ref. [2]. Concerning the oscillator we found that the system lays in the regime $\hbar\omega_0 \ll \hbar\Gamma_e \ll k_B T$, where we recall that ω_0 is the (bare) mechanical resonance frequency measured far from the conductance peaks. This implies that the oscillator can be described by a classical approach and that it is much slower than the electronic degrees of freedom. We will use then a Born-Oppenheimer kind of approximation, where one first solves the electronic problem for a given value of the displacement x of the oscillator and then considers the back-action of the electronic system on the oscillator [3–7].

We begin with the electronic description for the case of N_s electronic degrees of freedom, where $N_s = 1$ describes the spinless case, $N_s = 2$ the spin- or valley-degenerate case, and $N_s = 4$ the case when both valley and spin degeneracy are taken into account. We will find that most results do not depend on the actual value of N_s . In the incoherent transport regime ($k_B T \gg \hbar\Gamma_e$) the system is fully described by the probability that the electronic state σ (for instance σ could be the spin projection) is occupied: P_σ . We define also the probability that the dot is empty P_0 , or occupied by one of the σ states $P_1 = \sum_\sigma P_\sigma$. We assume that Coulomb blockade forbids double occupancy of the dot. One can then write a Pauli master equation for these probabilities:

$$\dot{P}_\sigma = \Gamma^+ P_0 - \Gamma^- P_\sigma. \quad (2)$$

Here $\Gamma^\pm = \Gamma_L^\pm + \Gamma_R^\pm$, and Γ_α^\pm is the rate at which an electron is added (+) or removed (-) from the quantum dot from the α ($=L, R$) lead. The probability satisfies the sum-rule $\sum_\sigma P_\sigma + P_0 = 1$. The explicit expression of the rates depends on the Fermi distributions on the leads: $\Gamma_\alpha^+ = \Gamma_\alpha f_\alpha$ and $\Gamma_\alpha^- = \Gamma_\alpha (1 - f_\alpha)$, where by symmetry the rates do not depend on σ . The electric current at the left lead and going from the left to the right lead, reads then:

$$I_L = -e [N_s \Gamma_L^+ (1 - P_1) - \Gamma_L^- P_1] \quad (3)$$

where we introduced the probability that the dot is occupied with one electron of any species $P_1 = \sum_\sigma P_\sigma$. The

equation of motion for the probability simplifies to

$$\dot{P}_1 = N_s \Gamma^+ - (N_s \Gamma^+ + \Gamma^-) P_1. \quad (4)$$

Using its stationary solution one finds that the current is

$$I_L = -e N_s (\Gamma_R^- \Gamma_L^+ - \Gamma_L^- \Gamma_R^+) / \Gamma_e, \quad (5)$$

where $\Gamma_e = N_s \Gamma^+ + \Gamma^-$. Setting the right lead to the ground as in the experiment and using V_g and V as the voltage potentials applied to the gate and the left lead, one can write the dependence of the Fermi distributions on these voltages: $f_L = f_F(\epsilon_1 - e(V_g - V)C_g/C_\Sigma + eVC_R/C_\Sigma)$ and $f_R = f_F(\epsilon_1 - eV_g C_g/C_\Sigma - eVC_R/C_\Sigma)$, where C_L , C_R , C_g are the left, right and gate capacitances, $C_\Sigma = C_L + C_R + C_g$, $f_F(\epsilon) = 1/(e^{\epsilon/k_B T} + 1)$, and $\epsilon_1 = \epsilon_0 + (e^2 - 2Qe)/2C_\Sigma$, with Q the total charge on the dot, and ϵ_0 the single electron energy.

We can now calculate the conductance for vanishing bias voltage:

$$G = -\frac{\Gamma_L \Gamma_R N_s e^2}{(\Gamma_L + \Gamma_R)[1 + (N_s - 1)f_0]} \frac{\partial f_0}{\partial \epsilon_1} \quad (6)$$

where we introduced $f_0 = f_L = f_R$ for $V = 0$. The conductance has a maximum when the argument of the Fermi function equals $k_B T \ln N_s/2$.

C. Back-action on the oscillator

We now consider the coupling of the quantum dot to the oscillator. When one electron is added to the dot, an additional electrostatic force F_e acts on the oscillator leading to a term in the Hamiltonian $-F_e x n$, where n is the additional number of electrons on the dot. In the incoherent regime n can only take the integer values 0 or 1. (In the main text we used the usual notation found in the opto-mechanical literature for the coupling $\hbar g = F_e x_{zp}$, where $x_{zp} = \sqrt{\hbar/2m\omega_0}$ with m the mass of the oscillator.) The presence of this coupling term changes the previous equations in Sec. IB by introducing the following substitution in the rate expressions:

$$\epsilon_0 \rightarrow \epsilon_0 - F_e x. \quad (7)$$

We can then write a system of equations describing the oscillator position and the probability of occupation of the dot [8]:

$$m\ddot{x} = -m\omega_0^2 x - m\gamma\dot{x} + F_e P_1(t) + F(t) \quad (8)$$

$$\dot{P}_1(t) = N_s \Gamma^+(x) - \Gamma_e(x) P_1, \quad (9)$$

here γ and $F(t)$ are the intrinsic damping rate and a weak external force driving the oscillator.

Assuming small displacements from the equilibrium value of both x and P_1 we can define

$$x = x_0 + \tilde{x}(t) \quad (10)$$

$$P_1 = P_1^{(0)} + \tilde{P}_1(t). \quad (11)$$

We obtain the following non-linear equations for x_0 and $P_1^{(0)}$:

$$x_0 = \frac{F_e}{m\omega_0^2} P_1^{(0)} \quad (12)$$

$$P_1^{(0)} = \frac{N_s \Gamma^+(x_0)}{\Gamma_e(x_0)}, \quad (13)$$

and a linear system for the small fluctuating parts \tilde{x} and \tilde{P}_1 :

$$\ddot{\tilde{x}} = -\omega_0^2 \tilde{x} - \gamma \dot{\tilde{x}} + (F_e/m) \tilde{P}_1 + F(t)/m \quad (14)$$

$$\dot{\tilde{P}}_1 = [N_s \partial_x \Gamma^+ - P_1^{(0)} \partial_x \Gamma_e] \tilde{x} - \Gamma_e \tilde{P}_1. \quad (15)$$

Introducing the Fourier transform $\tilde{x}(\omega) = \int dt e^{i\omega t} \tilde{x}(t)$ and using the explicit form of $P_1^{(0)}$ we have:

$$\tilde{P}_1(\omega) (\Gamma_e - i\omega) = N_s (\Gamma^- \partial_x \Gamma^+ - \Gamma^+ \partial_x \Gamma^-) \tilde{x}(\omega). \quad (16)$$

Substituting this expression into the equation for the displacement we have

$$[-\omega^2 + \omega_Q^2 - i\omega\gamma_R] \tilde{x}(\omega) = F(\omega)/m \quad (17)$$

with the renormalized damping and frequency:

$$\gamma_R = \gamma - \frac{F_e^2 N_s}{m \Gamma_e} \Xi, \quad (18)$$

$$\omega_Q^2 = \omega_0^2 + \frac{F_e^2 N_s}{m} \Xi, \quad (19)$$

where we use the notation ω_Q since it is related to the quadratic coefficient of the effective potential. We defined

$$\Xi = \frac{\Gamma^- \partial_{\epsilon_1} \Gamma^+ - \Gamma^+ \partial_{\epsilon_1} \Gamma^-}{\omega^2 + \Gamma_e^2}. \quad (20)$$

More explicitly, we have:

$$\Xi = -\frac{1}{k_B T} \frac{(\Gamma_L + \Gamma_R) [\Gamma_L f_L (1 - f_L) + \Gamma_R f_R (1 - f_R)]}{\omega_0^2 + \Gamma_e^2}, \quad (21)$$

where we substituted ω by the value of the unperturbed resonance frequency ω_0 . Strictly speaking when the reduction of ω_Q is large one should insert ω_Q and obtain a self-consistent equation, but since we are interested in the limit of $\Gamma \gg \omega_0 > \omega_Q$ this will have a negligible impact on the final result. The expression simplifies further in the relevant limit $eV \ll k_B T$ used in the experiment:

$$\Xi = -\frac{1}{k_B T} \frac{(\Gamma_L + \Gamma_R)^2 f_0 (1 - f_0)}{\omega_0^2 + (\Gamma_L + \Gamma_R)^2 [1 + (N_s - 1) f_0]^2}, \quad (22)$$

where $f_0 = f_L = f_R$ is the Fermi distribution of the leads. For the damping we thus obtain

$$\gamma_R = \gamma + \frac{\epsilon_P}{k_B T} \frac{N_s \omega_0^2 (\Gamma_L + \Gamma_R) f_0 (1 - f_0)}{k (\omega_0^2 + (\Gamma_L + \Gamma_R)^2 k^2)}, \quad (23)$$

with $k = 1 + (N_s - 1)f_0$. We introduced the polaronic energy $\epsilon_P = F_e^2/m\omega_0^2 = 2\hbar g^2/\omega_0$, which is the crucial energy scale of the problem. For $\omega_0 \ll \Gamma_L + \Gamma_R$ the resonance frequency simplifies to

$$\omega_Q^2 = \omega_0^2 \left[1 - \frac{\epsilon_P}{k_B T} N_s \frac{f_0(1-f_0)}{[1 + (N_s - 1)f_0]^2} \right]. \quad (24)$$

The importance of the ratio $\epsilon_P/k_B T$ it is clearly visible here, since when this ratio is sufficiently large ω_Q^2 changes sign, indicating the appearance of a bistability. Note that f_0 is the Fermi distribution of the metal electrodes. One can readily verify that the resonance frequency associated with the linear part of the restoring force is lowest when $f_0 = 1/(1 + N_s)$. It reads

$$\omega_Q^2|_{\min} = \omega_0^2 \left[1 - \frac{\epsilon_P}{4k_B T} \right], \quad (25)$$

independently of N_s . Substituting the same value of $f_0 = 1/(N_s + 1)$ into the expression for the damping Eq. (23) for $\omega_0 \ll \Gamma_L + \Gamma_R$ one obtains

$$\gamma_R = \gamma + \frac{\epsilon_P}{k_B T} \frac{\omega_0^2}{4\Gamma_e}, \quad (26)$$

where $\Gamma_e = (\Gamma_L + \Gamma_R)N_s/(N_s + 1)$. Thus in terms of Γ_e the expression of the damping at the maximum of reduction of the frequency does not depend on N_s . This expression has been used to extract the value of Γ_e in the main text.

D. Effective potential

The reduction of the resonance frequency is due to the back-action of the electronic system on the oscillator. This generates an effective force acting on the oscillator that depends on x in a non-linear fashion due to the x -dependence of the tunnelling rate:

$$F_{\text{eff}}(x) = -m\omega_0^2 x + F_e N_s \Gamma^+(x)/\Gamma_e(x). \quad (27)$$

Here $\Gamma^+(x)$ and $\Gamma_e(x)$ are defined in Sec. IB using $\epsilon_0 \rightarrow \epsilon_0 - F_e x$. In the equilibrium case ($eV \ll k_B T$) the force reads:

$$F_{\text{eff}}(x) = -m\omega_0^2 x + \frac{F_e}{e^{(\epsilon - F_e x)/k_B T} - \ln N_s + 1}, \quad (28)$$

where $\epsilon = \epsilon_1 - eV_g C_g/C_\Sigma$. The electronic contribution is clearly non-linear. The interpretation is simple. The force induced by the electrons is just F_e multiplied by the probability that the dot is occupied by an additional electron. In equilibrium this probability is given by the Fermi function. Note however that it does not coincide with the Fermi distribution of the metals (f_0), since the chemical potentials in the dot and in the leads differ. The number of electronic degrees of freedoms N_s appear only

as a shift of the energy level. The equilibrium condition for the mechanical oscillator $F_{\text{eff}}(x_0) = 0$ gives

$$m\omega_0^2 x_0 = \frac{F_e}{e^{(\epsilon - F_e x_0)/k_B T} - \ln N_s + 1}. \quad (29)$$

The spring constant is proportional to the derivative with respect to x_0 of the right-hand side of this expression. It is maximal for

$$(\epsilon_M - F_e x_0)/k_B T = \ln N_s. \quad (30)$$

When sweeping the gate voltage, that is ϵ , the resonance frequency reaches its minimum at ϵ_M . (One can show that the energies ϵ corresponding to the maximum of the conductance and to the maximum of the reduction of the frequency coincide only in the case of spin-less fermions $N_s = 1$; the difference in ϵ is however of the order of $k_B T \ln N_s$ and is thus difficult to resolve experimentally.) In terms of the displacement from the equilibrium value, $\tilde{x} = x - x_0$, the effective force acquires a particularly simple form:

$$F_{\text{eff}}(\tilde{x}) = -m\omega_0^2 \tilde{x} + \frac{F_e}{2} \tanh \left[\frac{F_e \tilde{x}}{2k_B T} \right]. \quad (31)$$

We can then obtain the effective potential by integration:

$$U_{\text{eff}}(\tilde{x}) = \frac{m\omega_0^2 \tilde{x}^2}{2} - k_B T \ln \left[\cosh \left[\frac{F_e \tilde{x}}{2k_B T} \right] \right], \quad (32)$$

where we choose the arbitrary potential constant such that $U_{\text{eff}}(0) = 0$. The potential is symmetric in this case [when Eq. (30) holds], the general form can be readily derived by integrating Eq. (31).

From Eq. (32) one can see that the effective potential evolves from a purely parabolic behaviour for F_e small to a double well for F_e sufficiently large. It is interesting to write the potential in terms of the dimensionless variable $z = \tilde{x}/(F_e/m\omega_0^2)$, that measures the distances in units of the displacement induced by the force F_e . The potential reads:

$$\frac{U_{\text{eff}}}{\epsilon_P} = \frac{z^2}{2} - \frac{1}{\tilde{\epsilon}_P} \ln \cosh(\tilde{\epsilon}_P z/2). \quad (33)$$

One can see that its form depends now on a single parameter $\tilde{\epsilon}_P = \epsilon_P/k_B T$, that is the natural coupling constant of the problem. We show in Fig. S2 the evolution of the potential for $\tilde{\epsilon}_P = 0.1, 2, 4, 6, 10$. One can expand the potential to order 4 to obtain:

$$\frac{U_{\text{eff}}}{\epsilon_P} = \frac{z^2}{2} \left(1 - \frac{\tilde{\epsilon}_P}{4} \right) + \frac{\tilde{\epsilon}_P^3}{192} z^4 + \dots \quad (34)$$

For $\tilde{\epsilon}_P \ll 1$, one has a simple harmonic oscillator. For $\tilde{\epsilon}_P = 4$ the quadratic term vanishes and for small displacement the potential is quartic at leading order. For $\tilde{\epsilon}_P > 4$ the system is bistable and features a double-well potential.

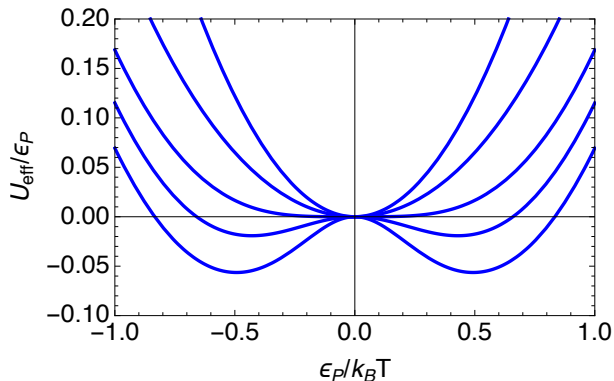


Fig. S2: Evolution of the effective potential for the oscillator for different values of the ratio $\epsilon_P/k_B T = 0.1, 2, 4, 6, 10$ from the upper to the lower curve. For $\epsilon_P/k_B T = 4$ the potential is quartic at leading order.

The bistability is directly related to the two possible states of the dot, empty or filled with one electron. The phase diagram and the crossover to the bistability in the coherent tunnelling limit has been discussed in Refs. [9, 10]. In the bistable region the current is strongly reduced leading to a current blockade induced by the electron-phonon coupling. Recently it has been proposed to exploit this kind of bistability in a double-dot coupled to an oscillator to design a nanomechanical qubit[11].

E. Fluctuation spectrum and softening of the mechanical mode

The first effect of the coupling is a reduction of the resonance frequency. For small $\tilde{\epsilon}_P$ or for small displacement this follows from the expression of the quadratic part of the effective potential (Eq. 34) that leads to

$$\frac{\omega_Q^2}{\omega_0^2} = 1 - \frac{\tilde{\epsilon}_P}{4} \quad \text{for } \tilde{\epsilon}_P \ll 1. \quad (35)$$

This effect has been observed by several groups [12–18]. For larger values of $\tilde{\epsilon}_P$ one cannot rely anymore on just the value of the quadratic part to quantify the observed mechanical resonance frequency. The oscillator becomes highly non-linear, so some care has to be taken to measure the resonance frequency of the system in equilibrium. This can be done by measuring the driven spectrum by keeping the driven vibration amplitude smaller than the standard deviation of the thermal vibration amplitude. Otherwise, the resonance frequency depends on the intensity of the drive used to detect it, see Sec. I G. Even for infinitesimal drive, the thermal fluctuations allow to explore regions of different vibration amplitudes for which the period of the oscillator takes values that can be very different. In order to find an averaged value for the observed resonance frequency for small drive we

will follow again Ref. [9] and calculate the displacement fluctuation spectrum at equilibrium:

$$S_{xx}(\omega) = \int dt e^{i\omega t} \langle (\tilde{x}(t) - \langle \tilde{x} \rangle)(\tilde{x}(0) - \langle \tilde{x} \rangle) \rangle. \quad (36)$$

For a small coupling constant $S_{xx}(\omega)$ reduces to a Lorentzian function peaked at ω_Q as defined in Eq. (35). For a larger coupling constant the resonance peak broadens and shifts to lower frequencies, but it remains well identified, and the resonance frequency can be determined for instance, by measuring $S_{xx}(\omega)$ [19]. In Ref. [9] it is shown that in the equilibrium limit $S_{xx}(\omega)$ coincides with the response function for a weak drive, which is what is measured in this work. In equilibrium and for infinitesimal damping, $S_{xx}(\omega)$ can be calculated following the methods of statistical mechanics [20]:

$$S_{xx}(t) = \int d\tilde{x}_o dp_o P(\tilde{x}_o, p_o) [\tilde{x}(t)\tilde{x}(0) - \langle \tilde{x} \rangle^2], \quad (37)$$

where $\tilde{x}(t)$ is the solution to the time evolution of the displacement when the force is given by F_{eff} in Eq. (31) with initial conditions for the displacement and the momentum \tilde{x}_o and p_o . The quantity P is the Boltzman distribution:

$$P(\tilde{x}_o, p_o) = \mathcal{N} e^{-\frac{p_o^2/2m + U_{\text{eff}}(\tilde{x}_o)}{k_B T}} \quad (38)$$

where U_{eff} is given by Eq. (32) and \mathcal{N} is a normalization factor.

In order to perform the calculation it is convenient to change the integration variables. Instead of using (\tilde{x}_o, p_o) we will use (E, τ) , where $E = p_o^2/2m + U(\tilde{x}_o)$ and τ is the time along the trajectory of energy E . The Jacobian is unitary $d\tilde{x}_o dp_o = dE d\tau$. We can now write the spectrum as follows:

$$S_{xx}(t) = \int dE \int_0^{T_E} d\tau_E e^{-E/k_B T} \mathcal{N} \tilde{x}_E(t + \tau_E) \tilde{x}_E(\tau_E) \quad (39)$$

where τ_E is the time along the trajectory with energy E and T_E is the period of the orbit. Note that one could have more than one orbit for a given energy. We will focus in the following on the stable case occurring when $\tilde{\epsilon}_P < 4$ and for which only one orbit is present. We can now perform the Fourier transform of Eq. (39) by introducing the Fourier series of the orbit displacement:

$$\tilde{x}_E(\tau) = \sum_{n=-\infty}^{+\infty} e^{-in\omega_E \tau} \tilde{x}_n(E) \quad (40)$$

$$\tilde{x}_n(E) = \int_0^{T_E} \frac{d\tau}{T_E} e^{in\omega_E \tau} x_E(\tau) \quad (41)$$

with $\omega_E = 2\pi/T_E$. Substituting these expressions into Eq. (39) and performing the Fourier transform we obtain:

$$S_{xx}(\omega) = \mathcal{N} \int dE e^{-E/k_B T} \sum_{n \neq 0} |\tilde{x}_n(E)|^2 T_E 2\pi \delta(\omega - n\omega_E).$$

(42)

Note that dropping the $n = 0$ harmonics allows to subtract the average of the trajectory.

We now perform the integral in the energy variable. The equation $n\omega_{E_n(\omega)} = \omega$ defines a function $E_n(\omega)$ for each trajectory. We can then write:

$$S_{xx}(\omega) = \mathcal{N} e^{-E_n(\omega)/k_B T} \sum_{n \neq 0} |\tilde{x}_n(E_n(\omega))|^2 \frac{2\pi n}{\omega} \frac{2\pi}{n \left| \frac{d\omega_E}{dE} \right|} \quad (43)$$

This expression can be used to compute the spectrum either numerically for any value of the parameters, or analytically in some limits. In Fig. S1 we show the result of the numerical evaluation of this expression for $\tilde{\epsilon}_P < 4$. For $\tilde{\epsilon}_P > 4$ the system becomes bistable; the crossover between the stable and the bistable regions occurs when the quadratic term of the effective potential vanishes, see the dotted yellow line in Fig. S1. Due to the strong non-linearity of the potential combined with the thermal fluctuations, the spectrum has a maximum corresponding to the resonance frequency (thick red continuous line), which approaches $\approx 0.75\omega_0$ at $\tilde{\epsilon}_P = 4$. The spectrum in Fig. S1 also shows a large broadening of the resonance due to phase fluctuations. The effective quality factor approaches $Q \simeq 5.5$ at $\tilde{\epsilon}_P = 4$. Note that there is no direct contribution of the dissipation to the peak broadening in the model. Taking into account the dissipation induced by the coupling between vibrations and single-electron tunneling (SET) changes only qualitatively the peak broadening in Fig. S1.

The dependence of the maximum of this spectrum as a function of $\tilde{\epsilon}_P$ has been used in the main text (see Fig. 2c) to fit the temperature dependence of the resonance frequency at the gate voltage corresponding to the conductance peak and infer an estimate of ϵ_P . We do not have an analytical expression, but fitting the numerical result one obtains

$$\omega_M/\omega_0 = 1 + \sum_{n=1}^5 a_n \tilde{\epsilon}_P^n \quad (44)$$

with $a_1 = -0.127655$, $a_2 = 0.010475$, $a_3 = 0.0125029$, $a_4 = -0.00480876$, and $a_5 = 0.000515142$, which is within 0.1% of the numerical result for $0 \leq \tilde{\epsilon}_P \leq 4$.

F. Coefficients of a series expansion of the potential in the displacement and estimation of the thermal energy stored in the non-harmonic part of the potential

In this section we derive explicit expressions for the first 4 coefficients of the series expansion of the effective potential for small \tilde{x} . We will express these nonlinear coefficients as well as the amount of thermal energy stored in the nonlinearity as a function of ϵ_P . This allows us

to quantify the amount of thermal energy stored in the nonlinearity shown in Fig. 4d from the suppression of the resonance frequency measured at each temperature in the main text using Eq. 44. We will use the standard notation:

$$U_{\text{eff}}(\tilde{x}) = U_0 + \frac{m\omega_Q^2}{2} \tilde{x}^2 + \frac{m\beta_D}{3} \tilde{x}^3 + \frac{m\gamma_D}{4} \tilde{x}^4. \quad (45)$$

Since the constant is irrelevant, we can obtain the other coefficients directly from the expression of the effective force Eq. (31) using $dU_{\text{eff}}/dx = -F_e n + m\omega_0^2 x$, $d^2U_{\text{eff}}/dx^2 = -F_e dn/dx + m\omega_0^2$, and so on. Here $n = 1/(\exp\{(\epsilon - F_e x)/k_B T - \ln N_s\} + 1)$ and has to be evaluated at $x = x_0$, that is, the equilibrium position. Using the properties of n we have:

$$\frac{\omega_Q^2}{\omega_0^2} = 1 - \frac{\epsilon_P}{k_B T} n(1-n) \quad (46)$$

$$\beta_D = \frac{F_e^3}{2m(k_B T)^2} n(1-n)(2n-1) \quad (47)$$

$$\gamma_D = -\frac{F_e^4}{6m(k_B T)^3} n(1-n)(6n^2 - 6n + 1). \quad (48)$$

We evaluate explicitly these expressions at the symmetric point for which $n = 1/2$:

$$\frac{\omega_Q^2}{\omega_0^2} = 1 - \frac{\epsilon_P}{4k_B T}, \quad \beta_D = 0, \quad (49)$$

$$\gamma_D = \frac{F_e^4}{48m(k_B T)^3} = \frac{\epsilon_P^2 m \omega_0^4}{48(k_B T)^3}. \quad (50)$$

These expressions are independent of the value of N_s .

In order to quantify the degree of non-linearity of the potential it is interesting to compare the contribution of the average of the quadratic term of the potential to the average of the full effective potential. For this we can use the expression of the effective potential given by Eq. (33). The average value of z^2 reads:

$$\langle z^2 \rangle = \int dz e^{-U_{\text{eff}}(z)/\tilde{\epsilon}_P} z^2 \Big/ \int dz e^{-U_{\text{eff}}(z)/\tilde{\epsilon}_P} = 1/\tilde{\epsilon}_P + 1/4. \quad (51)$$

Thus the average of the (dimensionless) quadratic part of the potential reads:

$$U_2 \equiv \frac{d^2 U_{\text{eff}}}{dz^2} \left\langle \frac{z^2}{2} \right\rangle = (1 - \tilde{\epsilon}_P/4)(1/\tilde{\epsilon}_P + 1/4)/2. \quad (52)$$

In a similar way we can calculate the average of the full potential

$$\langle U_{\text{eff}} \rangle = \int dz e^{-U_{\text{eff}}(z)/\tilde{\epsilon}_P} U_{\text{eff}}(z) \Big/ \int dz e^{-U_{\text{eff}}(z)/\tilde{\epsilon}_P}. \quad (53)$$

The quantity $\langle U_{\text{eff}} \rangle - U_2$ corresponds to the average of the sum of all the nonlinear terms of the potential, which

could be interpreted as the amount of thermal energy stored in the nonlinearity. One finds numerically that $\langle U_{\text{eff}} \rangle - U_2 \approx 0.0169\tilde{\epsilon}_P + 0.001\tilde{\epsilon}_P^2$ in the region $0 < \tilde{\epsilon}_P \leq 4$. This quantity is finite at $\tilde{\epsilon}_P = 4$ where U_2 vanishes. Thus, approaching this value the sum of the contribution of the non-linear terms becomes dominant with respect to the contribution of the quadratic term. A plot of $(\langle U_{\text{eff}} \rangle - U_2)/U_2$ as a function of $\tilde{\epsilon}_P$ is shown in Fig. S3. $(\langle U_{\text{eff}} \rangle - U_2)/U_2 \approx 0.033\tilde{\epsilon}_P^2$ for $\tilde{\epsilon}_P \rightarrow 0$ and $(\langle U_{\text{eff}} \rangle - U_2)/U_2 \approx 1.34/(4 - \tilde{\epsilon}_P)$ for $\tilde{\epsilon}_P \rightarrow 4$, the bistability threshold.

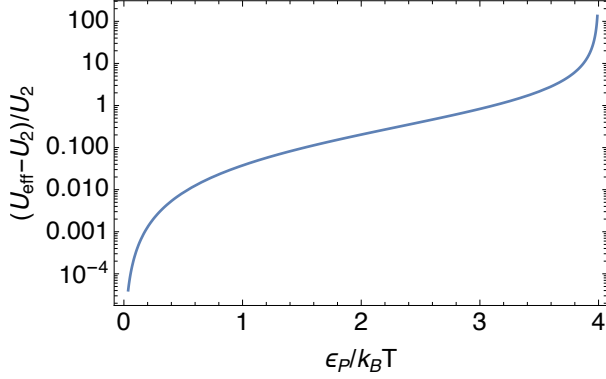


Fig. S3: Fraction of thermal energy stored in the nonlinearity, *i.e.* the ratio of the average of the sum of the non-linear terms of the potential to the average of the quadratic part U_2 .

G. Nonlinear Duffing response in presence of thermal fluctuations

In this subsection we consider the response of the non-linear oscillator to an external drive. The results of this section are used to extract the value of the coupling g from the measurement of the shift of the resonance frequency as a function of the driven vibration amplitude in Fig. 4b of the main text and to perform the fit of the response spectrum. The measurements are performed as close as possible to the symmetric point, for which the potential is symmetric in \tilde{x} . We will thus focus on this symmetric point, limiting the expansion to the quartic term. This corresponds to the standard Duffing oscillator in presence of thermal fluctuations. We find that the typical thermal amplitude of fluctuations of the oscillator are sufficiently large to induce a sizable change in the resonance frequency. It is thus crucial to include these fluctuations that modify quantitatively the nonlinear response to an external drive.

We will follow standard methods to describe the system [20, 21]. For clarity and uniformity of notation, we derive the main equations that lead to a Fokker-Planck description (see Eq. (70) in the following) of the slow degrees of freedoms: the two quadratures. We begin by

writing a Langevin equation for the displacement \tilde{x} :

$$\ddot{\tilde{x}} = -\gamma\dot{\tilde{x}} - \omega_0^2\tilde{x} - \gamma_D\tilde{x}^3 + f_D \cos(\omega t) + f_N(t), \quad (54)$$

where γ_D is the non-linear Duffing coefficient, and f_D and $f_N(t)$ are the driving and thermal forces divided by the mass. We assume

$$\langle f_N(t)f_N(t') \rangle = 2D\delta(t-t') \quad (55)$$

with $D = k_B T \gamma / m$. We now introduce the complex (quadrature) variable $z(t)$ as follows:

$$\tilde{x}(t) = z(t)e^{i\omega t} + z(t)^*e^{-i\omega t} \quad (56)$$

$$\dot{\tilde{x}}(t) = i\omega [z(t)e^{i\omega t} - z(t)^*e^{-i\omega t}]. \quad (57)$$

We can now perform the derivative of the above two equations:

$$\dot{\tilde{x}}(t) = i\omega [z(t)e^{i\omega t} - z(t)^*e^{-i\omega t}] \quad (58)$$

$$\ddot{\tilde{x}}(t) = 2i\omega\dot{z}(t)e^{i\omega t} + (i\omega)^2 [z(t)e^{i\omega t} + z(t)^*e^{-i\omega t}] \quad (59)$$

where we have used the condition $\dot{z}(t)e^{i\omega t} + \dot{z}(t)^*e^{-i\omega t} = 0$ implicit in the definition of z . Substituting the equations for \tilde{x} , $\dot{\tilde{x}}$, and $\ddot{\tilde{x}}$ in the equation of motion, multiplying it by $e^{-i\omega t}$, and averaging it over a period with the assumption that z evolves slowly gives

$$2i\omega\dot{z}(t) = \omega^2 z(t) - i\gamma\omega z(t) - \omega_0^2 z(t) - 3\gamma_D |z|^2 z(t) + \frac{f_D}{2} + \langle f_N(t)e^{-i\omega t} \rangle. \quad (60)$$

We now introduce the time variable $\tau = \gamma t / 2$ and scale z as $q(\tau) = \sqrt{3\gamma_D / \omega\gamma} z(2\tau/\gamma)$. This gives

$$\dot{q}(\tau) = -i\Omega q(\tau) - q(\tau) + i|q|^2 q(\tau) - iF_0 - iF_N(\tau), \quad (61)$$

where we approximated $\omega^2 - \omega_0^2 \approx 2\omega(\omega - \omega_0)$ and defined

$$\Omega = \frac{(\omega - \omega_0)}{\gamma/2}, \quad F_0 = \frac{\sqrt{3\gamma_D} f_D}{2(\omega\gamma)^{3/2}}, \quad (62)$$

$$F_N(t) = \left\langle \frac{\sqrt{3\gamma_D} f_N(t) e^{-i\omega t}}{(\omega\gamma)^{3/2}} \right\rangle. \quad (63)$$

Neglecting the fluctuations, the stationary solution reads

$$q_0 = F_0 / (|q_0|^2 - \Omega + i). \quad (64)$$

This defines the usual Duffing response. In particular one can express the dimensionless resonance frequency as a function of the amplitude:

$$\Omega = |q_0|^2 \pm \sqrt{F_0^2 / |q_0|^2 - 1}. \quad (65)$$

The first term defines what is called the 'back-bone' of the resonance. This corresponds roughly to the dependence of the maximum of the amplitude oscillation on the

driving frequency when measuring the spectra for different drives. It depends quadratically on the dimensionless oscillation amplitude. When the thermal fluctuations are negligible this dependence can be used to extract the value of the non-linear Duffing coefficient from the data. We discuss in the following the validity of this relation in presence of large thermal fluctuations.

We can now introduce $q = u + iv$, with u and v real. We have then

$$\dot{u} = g_u(u, v) + \xi_u(\tau), \quad \dot{v} = g_v(u, v) + \xi_v(\tau), \quad (66)$$

with

$$\xi_u + i\xi_v = -i\sqrt{3\gamma D} \langle f_N(t)e^{i\omega t} \rangle / (\omega\gamma)^{3/2}. \quad (67)$$

and

$$g_u = -u - (u^2 + v^2 - \Omega)v, \quad g_v = -v + (u^2 + v^2 - \Omega)u - F_0. \quad (68)$$

The correlation functions of the ξ -fields can be approximated by $\langle \xi_u(\tau)\xi_v(\tau') \rangle = 0$, $\langle \xi_u(\tau)\xi_u(\tau') \rangle = \langle \xi_v(\tau)\xi_v(\tau') \rangle = 2D\delta(\tau - \tau')$ where

$$D = \frac{3\gamma_D D}{4\omega^3\gamma^2} = \frac{3\gamma_D k_B T}{4m\omega^3\gamma}. \quad (69)$$

Finally from the two Langevin equations for u and v we can derive a Fokker-Planck equation for the probability $W(u, v)$:

$$D(\partial_u^2 + \partial_v^2)W - \partial_u(g_u W) - \partial_v(g_v W) = \partial_t W. \quad (70)$$

The Fokker-Planck Eq. (70) can be solved numerically for a given set of parameters to obtain the function

$$q_0(F_0, D, \Omega) = u_0 + iv_0 = \int dudv W(u, v)(u + iv). \quad (71)$$

This gives the average of the two quadratures in dimensionless units.

As a first application of this equation we calculate numerically the maximum of the response amplitude of the oscillator $|q_0^{\max}|$ and the value Ω_{\max} for which this maximum appears. When fluctuations are negligible, for $D \rightarrow 0$, from Eq. (65) one has $\Omega_{\max} = |q_0^{\max}|^2$. In Fig. S4 we plot Ω_{\max} as a function of $|q_0^{\max}|$ for different values of D . For the smallest value of $D = 0.1$ a good parabolic behavior is observed. Increasing D the curves flatten and deviations from the simple quadratic behavior are visible. This shows that using the quadratic dependence of the back-bone to extract the Duffing coefficient gives a qualitatively reasonable result when $D < 1$. In order to have a more reliable estimate, in the next subsection we discuss a fitting procedure that exploits the form of the response spectrum as predicted by the Fokker-Planck approach.

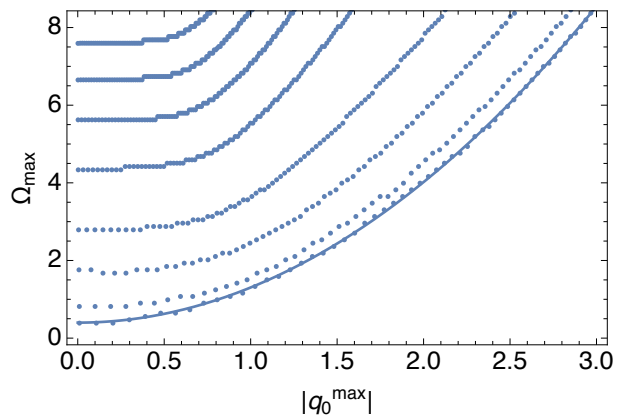


Fig. S4: The Figure shows Ω_{\max} as a function of $|q_0^{\max}|$ for $D = .1, .2, .5, 1., 2., 3., 4., 5.$, from the lower to the upper curve. The effect of the fluctuations is to shift the initial value to higher frequency and to deform the dependence on $|q_0^{\max}|$. In the case of $D = .1$ we show a fit with a quadratic dependence that gives a coefficient of $0.9|q_0^{\max}|^2$. The small steps are due to the discretization of the frequency in the numerical calculation.

H. Procedure used to fit the nonlinear Duffing response

Using the results described in the previous sub-section, we now explain the procedure to determine the Duffing constant, and thus the ratio $\epsilon_P/k_B T$ and the coupling g , from driven nonlinear spectra when the thermal fluctuations are large. These data are shown in Figs. 4a,c in main text and Fig. S5. We obtain the Duffing constant by collectively fitting the whole set of measured spectra spanning the linear-nonlinear crossover when sweeping the drive intensity. The spectra are measured nearby the conductance peak, that is, almost at the symmetric point. From the experimentally measured spectra, the two quadratures $\{U_{ni}, V_{ni}\}$ are extracted for N_v different values of the driving gate voltage V_n^{ac} and for N_w different values of the driving frequency ω_{ni} . One has thus a set of $2N_v N_w$ values with $N_v = 10$ and $N_w = 300$. Using the expression of the nonlinear coefficient given by Eq. (50) and the definition of D given by Eq. (69) we can write a dimensionfull expression of the quadratures $\{u_e, v_e\}$:

$$u_e = \frac{1}{\tilde{\epsilon}_P} \sqrt{\frac{k_B T \gamma}{m\omega_0^3}} u_0(F_0, \tilde{\epsilon}_P^2 \omega_0 / 64\gamma, (2\omega - \omega_0)/\gamma) \quad (72)$$

$$v_e = \frac{1}{\tilde{\epsilon}_P} \sqrt{\frac{k_B T \gamma}{m\omega_0^3}} v_0(F_0, \tilde{\epsilon}_P^2 \omega_0 / 64\gamma, (2\omega - \omega_0)/\gamma) \quad (73)$$

Here $u_0(F_0, D, \Omega)$ and $v_0(F_0, D, \Omega)$ are the (average of the) dimensionless quadratures obtained from the solution of the Fokker-Planck equation as defined by Eq. (71).

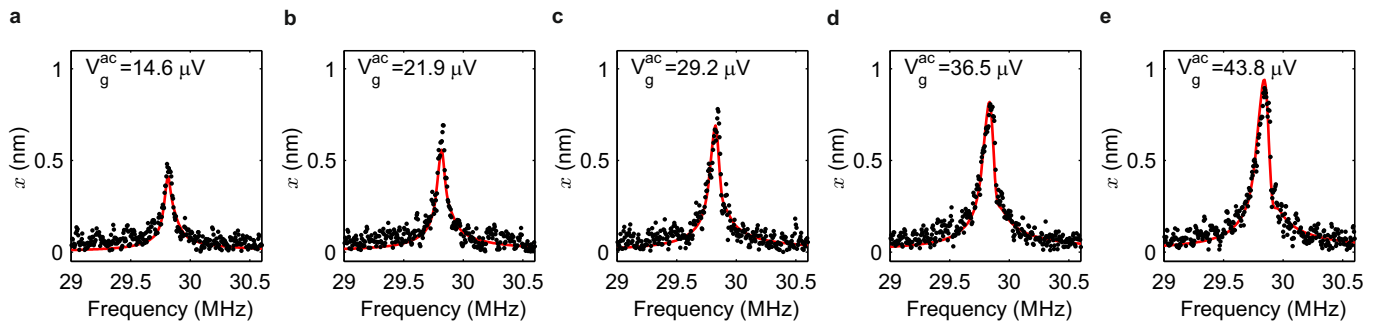


Fig. S5: Driven nonlinear spectra spanning the linear-nonlinear crossover when increasing the drive at 6 K. We emphasize that a single set of parameters is used to fit the data of 10 different spectra; the fit is shown by the red line.

We then define the χ^2 function:

$$\chi^2 = \sum_{n=1}^{N_v} \sum_{i=1}^{N_w} \left[(u_e(\omega_{ni}, F_0 = F_v V_n^{ac}) - U_{ni})^2 + (v_e(\omega_{ni}, F_0 = F_v V_n^{ac}) - V_{ni})^2 \right]. \quad (74)$$

The free parameters of the fit are $\{\omega_0, \gamma, \tilde{\epsilon}_P, F_v\}$. The factor F_v is the relation between the dimensionless driving force intensity and the experimental driving voltage. This only assumes that the driving force increases linearly with the amplitude of the injected ac drive. The best fit for $V_g^{dc} = 0.7572$ V gives the values $\epsilon_P/k_B T = 0.22$, $\omega_0/2\pi = 29.7696$ MHz, $\gamma/2\pi = 13.229$ kHz, $F_v = 2.10897 \cdot 10^5$ V $^{-1}$. The fit is shown in Fig. S5.

In order to determine the error bar of the estimated value of $\epsilon_P/k_B T$, we find numerically the minimum of χ^2 for a given value of $\epsilon_P/k_B T$ by tuning the other three parameters ω_0 , γ , and F_v (see Fig. S6). We estimate this

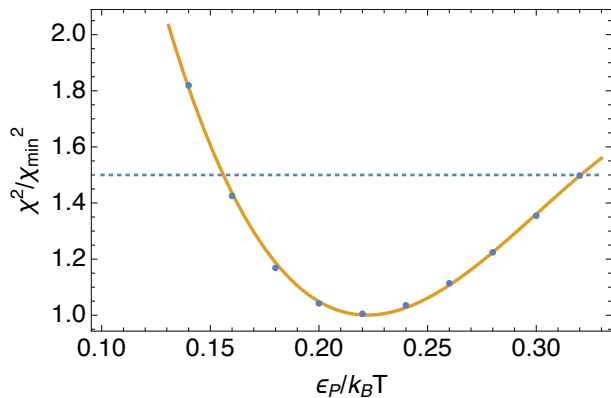


Fig. S6: Dependence of the χ^2 on $\epsilon_P/k_B T$.

error by finding the range in $\epsilon_P/k_B T$ for which $\chi^2(\epsilon_P) < 1.5\chi_{\min}^2$, where χ_{\min} is the minimum value of χ^2 . The value of 1.5 is chosen so that the probability of observing a χ^2 larger than this value is less than 1%. We find $0.15 < \epsilon_P/k_B T < 0.32$, which converts into a ± 120 MHz error

in the estimation of g . In addition to this error, one should include the imprecision in the calibration of the displacement, since the fit is very sensitive to the absolute value of the displacement. By performing the fit with different values of the displacement calibration, we found that $\Delta\epsilon_P/k_B T \approx 0.15\Delta A/A$, where ΔA is the systematic error in the measurement of the displacement amplitude. We estimate $\Delta A/A = 0.22$, which gives an additional ± 0.033 to the error bar for $\epsilon_P/k_B T$ (and ± 97 MHz error for $g/2\pi$). Overall, we get the coupling constant $g/2\pi = 646 \pm 217$ MHz.

II. EXPERIMENTAL SECTION

A. Device production

Carbon nanotubes are grown on high resistive silicon substrates with prefabricated platinum electrodes and trenches. The growth is done in the last step of the fabrication process to reduce surface contamination. Nanotubes are grown by the ‘fast heating’ chemical vapour deposition (CVD) method, which consists in rapidly moving the sample from a position outside of the oven to the center of the oven, so that the temperature of the sample rapidly grows from room temperature to about 850°C. This enables us to grow nanotubes over shallow trenches [22]. We remove the contamination molecules adsorbed on the nanotube surface during the transfer of the nanotube between the CVD oven and the cryostat, by applying a large current through the device under the ultra-high vacuum at the base temperature of the dilution cryostat [23]. In the three measured devices, the nanotube-gate separation is 150 nm and the length of the suspended nanotube is between 1.2 μm and 1.4 μm .

B. Electrical characterization

We select ultra-clean, small-gap semiconducting nanotubes. Figures S7a-c show charge stability diagram

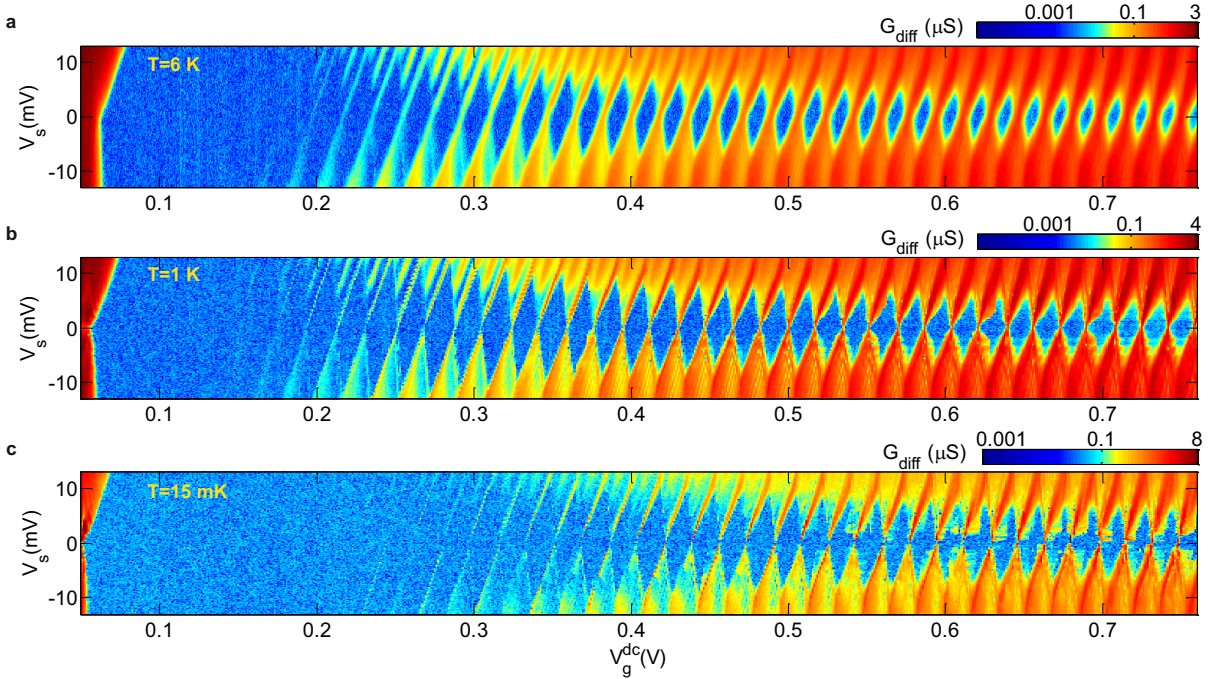


Fig. S7: Differential conductance of device I measured as a function of the source-drain voltage V_s and the gate voltage V_g^{dc} at different temperatures. The temperature of the cryostat is 6 K, 1 K, and 15 mK.

measurements at 6 K, 1 K, and the base temperature of the cryostat. The nanotube regions in contact with the source and drain electrodes are p-doped [24]. For large positive gate voltages, p-n junctions are formed along the nanotube near the metal electrodes, forming a quantum dot along the suspended nanotube. For gate voltage values below 0.05 V, the suspended nanotube region is p-doped and the p-n junctions disappear, resulting in a higher conductance. The size of the Coulomb diamonds decreases as the number of electrons in the nanotube quantum dot increases. The charging energy E_c varies approximately from 8.5 meV to 6.5 meV in the gate voltage range discussed in the main text, while the level spacing ΔE changes from 0.97 meV to 0.73 meV. All the data shown in the main text and supplementary materials are in the regime $k_B T < \Delta E, E_c$. The short separation between the nanotube and the gate electrode enables us to achieve a large capacitive coupling between the nanotube island and the gate electrode $C_g \gg C_s, C_d$, where C_s and C_d are the capacitances between the nanotube island and the source and drain electrode, respectively. The diamonds in the charge stability diagram measurements become distorted when lowering temperature due to the mechanical self-oscillations of the suspended nanotube generated at finite source bias voltages [13, 16, 17].

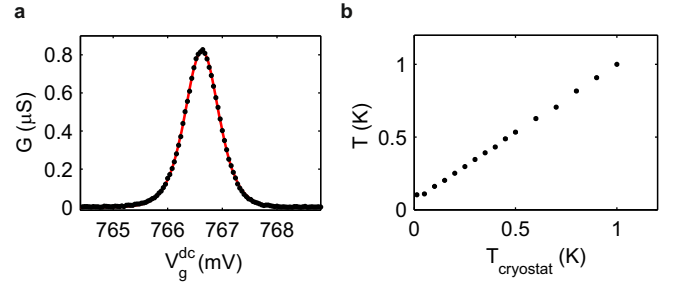


Fig. S8: Temperature calibration. (a) Gate voltage dependence of the conductance of device I at $T = 1$ K. The red solid line is the fit to the data using Eq. 75. (b) The electron temperature of the device measured as a function of the cryostat temperature.

C. Temperature calibration

The temperature calibration in quantum dot devices operated in the incoherent single-electron tunnelling regime ($\hbar\Gamma_e < k_B T < \Delta E, E_c$) is achieved by measuring the electrical conductance peak (Fig. S8a) where Γ_e is the electron coupling rate and T is the temperature. The electron temperature is obtained from the gate voltage V_g^{dc} width of the conductance peak using the standard incoherent single-electron tunnelling descrip-

tion [see Eq. (6) in Sec. IB]:

$$G = \frac{G_0}{\cosh^2 \left[\alpha (V_g^{\text{dc}} - V_P) / 2k_B T \right]}. \quad (75)$$

Here G_0 is the T -dependent peak conductance, α is the lever arm, and V_P is the gate voltage of the conductance peak. We checked with numerical calculations of the Fokker-Planck equation that the modification of the width of the conductance peak by the electromechanical coupling is negligible over the measured temperature range. Figure S8b shows that the electron temperature is linear with the cryostat temperature except at low temperature where it saturates at about 100 mK.

We cannot estimate the temperature of the mechanical vibration fluctuations by measuring their spectrum as a function of temperature, since the low mechanical Q -factor due to the electron tunnelling in the SET regime impedes us to resolve the resonance of thermal vibrations. In Ref. [16] we measured the vibration fluctuation temperature of a high- Q nanotube device as a function of cryostat temperature using the same cryostat and the same cabling, filters, and amplifier; we observed that the vibration temperature is linear with the cryostat temperature down to a saturation temperature that is similar to the electron saturation temperature in Fig. S8b. This indicates that the vibration temperature and the electron temperature are similar.

D. Detection of mechanical vibrations and estimation of the effective mass

We use a new two-source mixing method to measure the spectral mechanical response of driven vibrations in the linear and the nonlinear regimes. This method enables us to extract the spectral mechanical response by eliminating the inherent contribution of pure electrical origin in electrical mixing measurements [25]. We detect the vibrations by capacitively driving them with an oscillating voltage with amplitude V_g^{ac} and frequency ω , applying the oscillating voltage with amplitude V_g^{ac} with a slightly detuned frequency $\omega + \delta\omega$ on the source electrode, and measuring the current at frequency $\delta\omega$ from the drain electrode. To improve the sensitivity of the current detection, we connect the drain electrode to a RLC resonator placed nearby the device and a HEMT amplifier at the 4 K stage of the dilution cryostat [22]. The RLC resonator enables us to measure the current at a comparatively high frequency $\delta\omega \simeq 1.2$ MHz where the $1/f$ noise is significantly reduced. Without the inductance L of the RLC resonator, the frequency $\delta\omega$ has to be set to a lower frequency, typically 1 – 10 kHz, within the bandwidth imposed by the resistance of the sample and the capacitance of the electrical cables that connect the device to the measurement instruments. To obtain the spectral mechanical response of driven vibrations, we separate the signal of the mechanical vibrations from the

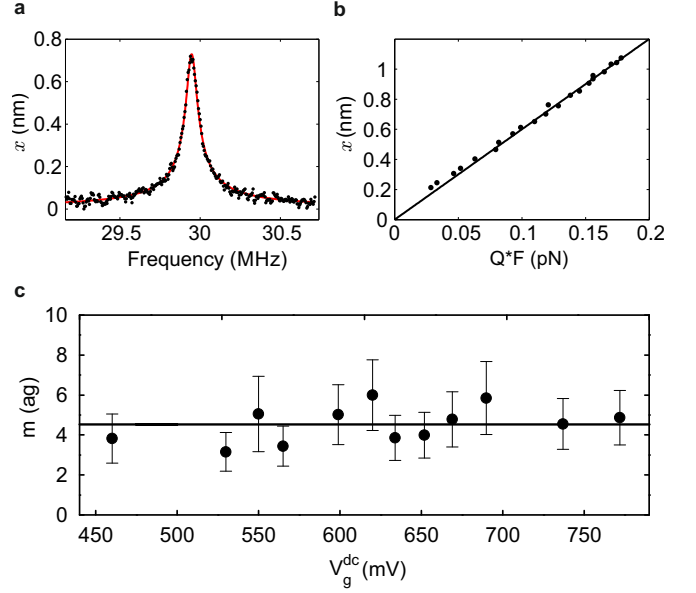


Fig. S9: Determination of the effective mass. (a) Spectral response of the displacement amplitude of the driven vibrations at $T = 6$ K. We chose the gate voltage close to the half maximum of the conductance peak, where the transconductance is largest. The red solid line is the fit of the data to a Lorentzian peak. (b) Force-displacement response curve at the mechanical resonance frequency. (c) Effective modal mass measured at different gate voltages. The black solid line indicates the average effective mass of 4.5 ag.

signal of pure electrical origin inherent to the mixing method by properly tuning the phase of the measured current [25]. This is important since the measured current is otherwise a non-trivial combination of the vibration displacement and the electrical contribution. The pure electrical contribution is used as a resource to calibrate the signal of the vibrations into units of meters. Figure S9a shows the spectral response of driven vibrations, which can be well described by a Lorentzian peak.

The effective mass of the measured mechanical eigenmode can be reliably determined, since the driven vibration amplitude can be calibrated with the two-source mixing method described above and since the capacitive force in quantum dot electromechanical devices can be accurately quantified. The mass m is quantified from the slope of the force-displacement (F - x) response at the mechanical resonance frequency in Fig. S9b using $x = (Q/m\omega_m^2)F$ where the quality factor Q is estimated from the spectral response in Fig. S9a and the capacitive force is given by

$$F = \beta C'_g V_g^{\text{dc}} V_g^{\text{ac}}, \quad (76)$$

$$\beta = 1 - \frac{C_g}{C_\Sigma} + f(1-f) \frac{C_g}{C_\Sigma} \frac{e^2/C_\Sigma}{k_B T}, \quad (77)$$

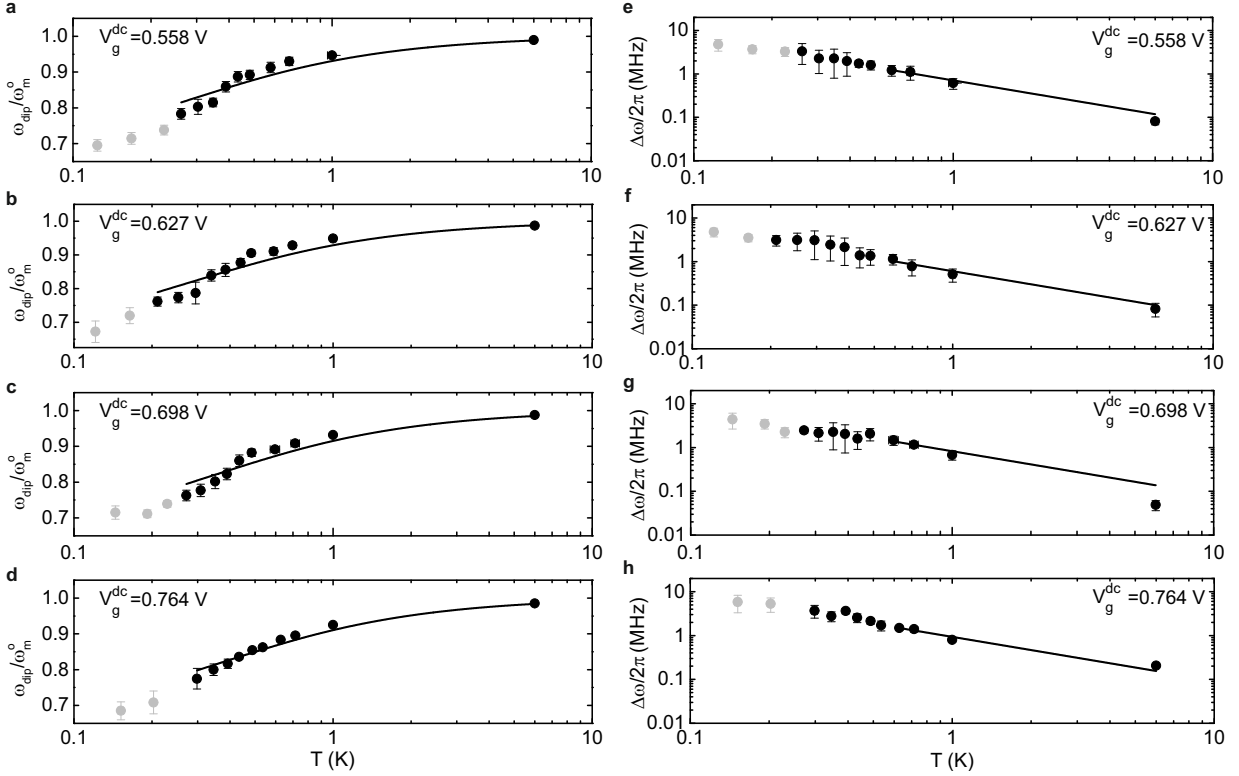


Fig. S10: Determination of the electromechanical coupling and the electron tunnel rate. (a)-(d) Temperature dependence of the mechanical resonance frequency ω_{dip} for different conductance peaks. We define ω_{dip} as the lowest resonance frequency when sweeping the gate voltage over a conductance peak (Fig. 2b of main text). The gate voltage of the resonance dip matches the gate voltage of the conductance peak. The black solid lines indicate the SET-based predictions. (e)-(h) Temperature dependence of the mechanical resonance width for different conductance peaks. The black solid lines indicate the SET-based predictions in the high temperature limit.

in the incoherent SET regime [25]. The dot-gate capacitance C_g , the total capacitance C_Σ of the dot, and the average charge occupation number f (with value between 0 and 1) are all quantified by standard electron transport measurements. The spatial derivative of the dot-gate capacitance C'_g is determined from C_g and the dot-gate separation d using the expression of the capacitance between a cylinder and a plate that leads to $C'_g = C_g/d \ln(2d/r)$. Figure S9c shows the effective mass measured at twelve different conductance peaks. The average effective mass is $m = 4.5 \pm 1.5$ ag. The uncertainty in the mass determination comes from the mass fluctuations in Fig. S9c and the uncertainty in the estimation of the dot-gate separation. We estimate the nanotube radius $r = 1.5$ nm from the measured mass and the suspended nanotube length determined by scanning electron microscopy. This value is consistent with the radii of the nanotubes produced with our chemical vapour deposition growth.

E. Electromechanical coupling and electron tunnel rate

Figures S10a-h show the temperature dependence of both the resonance frequency and the resonance width of driven vibrations measured at the conductance peaks for different gate voltages. The fitting of these data to the predictions of the theory enable us to determine the coupling g and the total electron tunnel rate Γ_e for these different conductance peaks. The values of g and Γ_e are shown in Figs. 3a,c of the main text. In the fitting we only select the black data points in Figs. S10a-d with resonance frequency ratios $\omega_{\text{dip}}/\omega_m^0$ between 0.75 and 1, since it is the range of values expected by the predictions discussed in Sec. IE. The grey data points correspond to data at lower temperature where a double-well potential is expected to emerge, but further work is needed to characterize this regime. The coupling of vibrations and SET also results in dissipation. The mechanical resonance width in the high temperature limit ($k_B T \gg \hbar g^2/\omega_m$) is given by

$$\Delta\omega = \Gamma_0 + \frac{1}{2} \frac{\hbar g^2}{k_B T} \frac{\omega_m^0}{\Gamma_e} \quad (78)$$

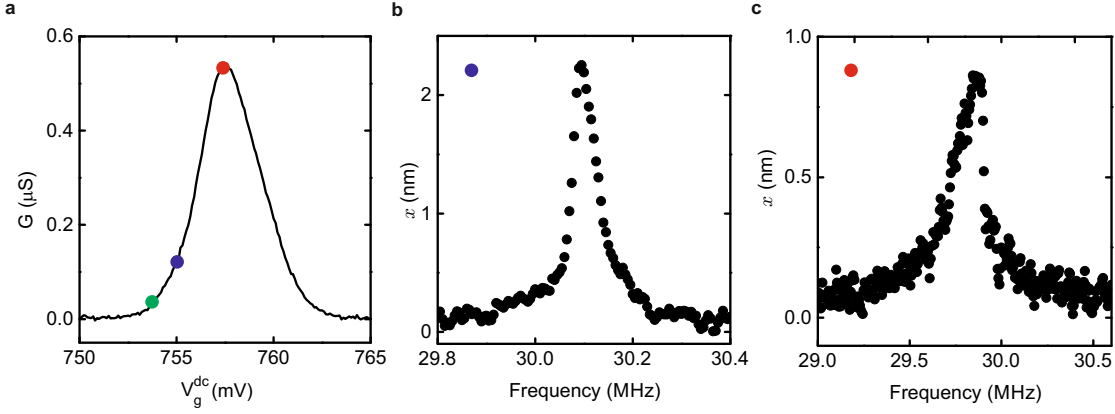


Fig. S11: Spring hardening and softening in the nonlinear spectral response of mechanical vibrations in Device I at 6 K. (a) Gate voltage dependence of the conductance. (b) Nonlinear response showing spring softening when the system is set at the base of the conductance peak (blue point). (c) Nonlinear response showing spring hardening when the system is set at the top of the conductance peak (red point).

where Γ_0 is the damping due to other dissipation mechanisms, see Eq. 26. We fit the measured resonance width in the high temperature limit with Eq. 78 in Fig. S10e-h. The electron tunnel rates Γ_e obtained from the fits are shown in Fig. 3c of the main text.

F. Nonlinear spectral response of mechanical vibrations

We show here that the nonlinear Duffing constant measured at 6 K changes sign when sweeping the gate voltage through the conductance peak, in agreement with the predictions of the theory in Sec. IF. This enables us to rule out other possible origins for the nonlinearity, such as the geometrical nonlinearity [26]. We observe both a softening and hardening spring behaviour of the oscillator over a narrow range in gate voltage, see Figs. S11a-c. Figure S11c shows the spectral response of the spring hardening when the system is set at the conduction peak as indicated by the red dot in Fig. S11a. By contrast, Fig. S11b shows the spring softening effect at the base of the conductance peak as highlighted by the blue dot in Fig. S11a. The change of the nonlinear Duffing sign is consistent with the predictions of the theory describing the coupling of mechanical vibrations and SET in the incoherent regime. Indeed, Eq. 48 indicates that the Duffing constant is positive at the conductance peak when the average charge occupation fraction $f = 1/2$, while it becomes negative at the base of the peak when f is sufficiently close to zero.

G. Responsivity of mechanical vibrations

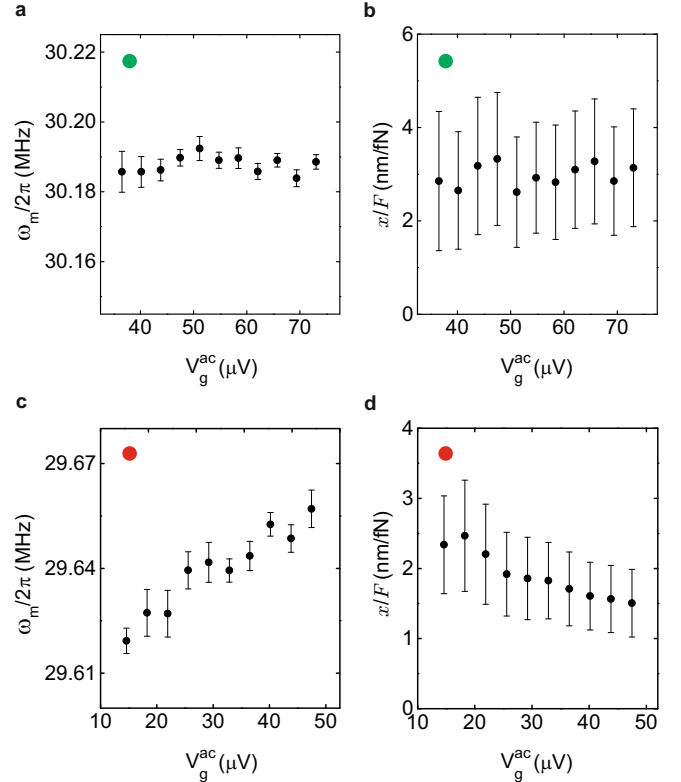


Fig. S12: Responsivity of mechanical vibrations at 6 K. (a,b) Resonance frequency and responsivity of the vibrations as a function of the driving voltage with the system set at the very base of the conductance peak in Fig. S11a (green dot). (c,d) Same as (a,b) but with the system set on the top of the conduction peak (red dot).

We show that the observed reduction of the responsivity at large drive is related to the thermal switching between coexisting stable states in driven nonlinear oscillators. Figures S12a,b show the drive dependence of both the mechanical resonance frequency and the responsivity of the mechanical vibrations when the system is set at the very base of the conductance peak, see green dot in Fig. S11a.

We do not observe any shift in resonance frequency, indicating that the Duffing constant is becoming small. This is expected from Eq. 48 when $f \simeq 0$, that is, when the effect of the coupling between vibrations and SET is suppressed. We do not observe any change of the responsivity either, showing that nonlinear damping plays a negligible effect [27].

By contrast, Fig. S12d shows that the responsivity gets lower when increasing the drive in the case where the system is set at the top of the conductance peak, see red dot in Fig. S11a. This reduction is well reproduced by the SET-based predictions (Fig. 4d in main text), which relates this behaviour to switching between coexisting stable states in driven nonlinear oscillators, and not to nonlinear damping.

H. Strong anharmonicity in two other devices

We demonstrate strong anharmonicity and ultra-strong coupling regime in two other devices. Figure S13a shows a conduction peak of Device II. The charging energy, the level spacing, and the electron tunnel rate are $E_c = 14$ meV, $\Delta E = 2$ meV, and $\hbar\Gamma_e = 2$ μ eV, respectively, showing that SET is in the incoherent regime ($\hbar\Gamma_e < k_B T < \Delta E, E_c$). The high lever arm $\alpha = 0.83$ arises from the short separation between the nanotube and the gate electrode. Figure S13b shows a dip with a large suppression of the mechanical resonance frequency when sweeping the gate voltage through the conductance peak; the bare resonance frequency is $\omega_m^o/2\pi = 35.1$ MHz. Figure S13c shows the temperature dependence of the mechanical resonance frequency at the dip. The ratio $\omega_{\text{dip}}/\omega_m^o$ approaches 0.75 at low temperature, indicating that the potential of the vibrations becomes strongly anharmonic. The red solid line is the fit of the data to the SET-based predictions, enabling us to quantify $g/2\pi = 384$ MHz. This value is similar to the value $g/2\pi = 395$ MHz obtained with independently measured parameters and using $g = e(C'_g/C_\Sigma)V_g^{\text{dc}}/\sqrt{2m\hbar\omega_m^o}$. These data indicate that the device is in the ultrastrong coupling ($g > \omega_m^o$) and the adiabatic regime ($\Gamma_e > \omega_m^o$), which satisfy the conditions to realize strong vibration anharmonicity. Figures S13d-f show the data of Device III. We obtain $g/2\pi = 529$ MHz and $\omega_m^o/2\pi = 89$ MHz, which shows that device is in the ultrastrong coupling regime. The measured suppression of the resonance frequency $\omega_{\text{dip}}/\omega_m^o$ reaches 0.93 at 500 mK. The device could not be measured at lower temperature due to technical problems unrelated to the de-

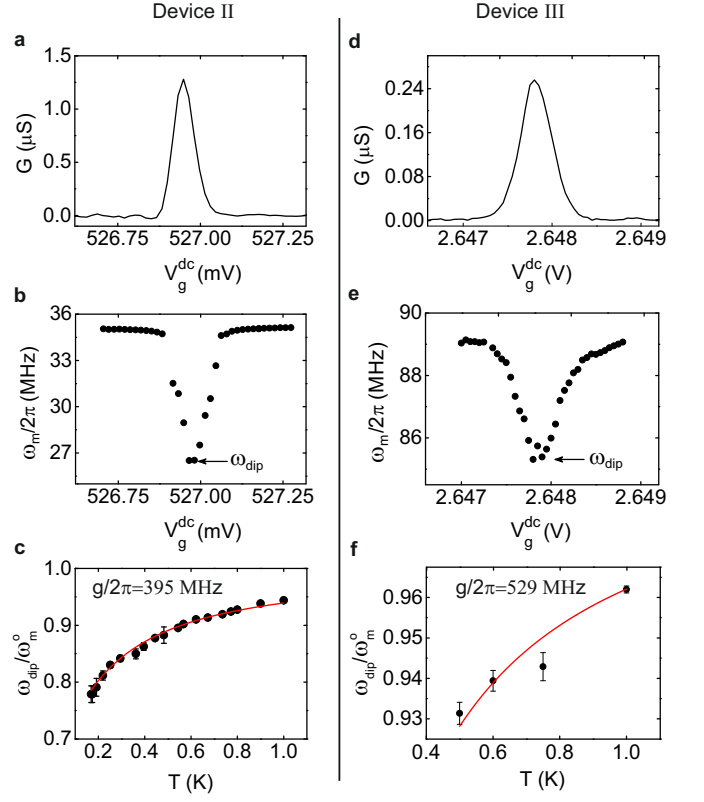


Fig. S13: Strong anharmonicity and ultra-strong coupling regime in two other devices. (a,b) Conductance and mechanical resonance frequency as a function of gate voltage at 170 mK for Device II. (c) Suppression of the resonance frequency as a function of temperature at the conduction peak. The solid red line is the SET-base prediction. (d,e) Conductance and mechanical resonance frequency as a function of gate voltage at 6 K for Device III. (f) Suppression of the resonance frequency as a function of temperature at the conduction peak.

vice itself. The anharmonicity is sizeable but not as large as that in Devices I and II.

I. Estimation of error bars in the figures of the main text

In Fig. 2 of the main text, the confidence interval error bars in panels (b) and (c) arise primarily from the standard deviation in ω_m quantified from different driven spectral response measurements. In Fig. 3 of the main text, the confidence interval error bars in panels (a) (black dots) and (c) arise primarily from the uncertainty in the fit of the measured temperature dependence of ω_m and $\Delta\omega$, respectively, to the predictions of the theory. The confidence interval in the estimation of g shown in (a) (purple shaded area) mainly originates from the uncertainty in the measurement of the mass. In Fig. 4 of

the main text, the confidence interval error bars in panels (b) and (c) arise from the uncertainty in the fitting of the spectral response and the determination of the dot-gate separation.

J. Parameters of Device I discussed in the main text

| Parameters | Device I |
|--|-------------------|
| Suspended nanotube length (L) | 1.2 μm |
| Nanotube radius (r) | 1.5 nm |
| Effective mechanical mode mass (m) | 4.5 ag |
| Bare resonance frequency ($\omega_m^o/2\pi$) | 28.3-30.3 MHz |
| Nanotube-gate separation (d) | 150 nm |
| Zero point fluctuation (x_{zp}) | 7.9 pm |
| Nanotube-gate capacitance (C_g) | 9.7 aF |
| Lever arm (α) | 0.4 – 0.5 |
| Charging energy (E_c) | 8.5 – 6.5 meV |
| Level spacing (ΔE) | 0.97 – 0.73 meV |
| Work function difference between nanotube and gate | 120 mV |

-
- [1] G. Micchi, R. Avriller, and F. Pistolesi, Phys Rev Lett **115**, 206802 (2015).
- [2] L. I. Glazman and M. Pustilnik, in *New Directions in Mesoscopic Physics (Towards Nanoscience)*, edited by R. Fazio, V. F. Gantmakher, and Y. Imry (Springer Netherlands, Dordrecht, 2003), pp. 93–115, ISBN 978-1-4020-1665-3 978-94-007-1021-4.
- [3] A. D. Armour, M. P. Blencowe, and Y. Zhang, Phys. Rev. B **69**, 125313 (2004), ISSN 1098-0121, 1550-235X.
- [4] Y. M. Blanter, O. Usmani, and a. Y. V. Nazarov, Phys. Rev. B. **93**, 136802 (2004), ISSN 0031-9007, 1079-7114.
- [5] Y. M. Blanter, O. Usmani, and a. Y. V. Nazarov, Phys. Rev. Lett. **94**, 049904 (2005), ISSN 0031-9007, 1079-7114.
- [6] D. Mozyrsky, M. B. Hastings, and I. Martin, Phys. Rev. B **73**, 035104 (2006), ISSN 1098-0121, 1550-235X.
- [7] F. Pistolesi and S. Labarthe, Phys. Rev. B **76**, 165317 (2007), ISSN 1098-0121, 1550-235X.
- [8] A. Benyamini, A. Hamo, S. V. Kusminskiy, F. von Oppen, and S. Ilani, Nat. Phys. **10**, 151 (2014), ISSN 1745-2473, 1745-2481.
- [9] G. Micchi, R. Avriller, and F. Pistolesi, Phys. Rev. Lett. **115**, 206802 (2015), ISSN 0031-9007, 1079-7114.
- [10] G. Micchi, R. Avriller, and F. Pistolesi, Phys. Rev. B **94**, 125417 (2016), ISSN 2469-9950, 2469-9969.
- [11] F. Pistolesi, A. N. Cleland, and A. Bachtold, Phys. Rev. X **11**, 031027 (2021).
- [12] B. Lassagne, Y. Tarakanov, D. Kinaret, J. and Garcia-Sanchez, and A. Bachtold, Science **325**, 1107 (2009).
- [13] G. A. Steele, A. K. Hüttel, B. Witkamp, M. Poot, H. B.

- Meerwaldt, L. P. Kouwenhoven, and H. S. J. van der Zant, *Science* **325**, 1103 (2009).
- [14] A. Benyamini, A. Hamo, S. V. Kusminskiy, F. von Oppen, and S. Ilani, *Nature Physics* **10**, 151 (2014).
- [15] I. Khivrich, A. A. Clerk, and S. Ilani, *Nature Nanotechnology* **14**, 161 (2019), ISSN 1748-3395.
- [16] C. Urgell, W. Yang, S. L. De Bonis, C. Samanta, M. J. Esplandiu, Q. Dong, Y. Jin, and A. Bachtold, *Nat. Phys.* **16**, 32 (2020).
- [17] Y. Wen, N. Ares, F. J. Schupp, T. Pei, G. A. D. Briggs, and E. A. Laird, *Nat. Phys.* **16**, 75 (2020).
- [18] S. Blien, P. Steger, N. Hüttner, R. Graaf, and A. K. Hüttel, *Nature Communications* **11**, 1636 (2020), ISSN 2041-1723, URL <https://doi.org/10.1038/s41467-020-15433-3>.
- [19] J. Moser, J. Güttinger, A. Eichler, M. J. Esplandiu, D. E. Liu, M. I. Dykman, and A. Bachtold, *Nature Nanotechnology* **8**, 493 (2013), ISSN 1748-3387, 1748-3395.
- [20] M. I. Dykman and M. A. Krivoglaz, *Physica A: Statistical Mechanics and its Applications* **104**, 480 (1980), ISSN 0378-4371.
- [21] M. I. Dykman and M. A. Krivoglaz, *Soviet. Phys. JETP* **50**, 30 (1979).
- [22] S. L. de Bonis, C. Urgell, W. Yang, C. Samanta, A. Noury, J. Vergara-Cruz, Q. Dong, Y. Jin, and A. Bachtold, *Nano Lett.* **18**, 5324 (2018), ISSN 1530-6984.
- [23] W. Yang, C. Urgell, S. L. De Bonis, M. Margańska, M. Grifoni, and A. Bachtold, *Phys. Rev. Lett.* **125**, 187701 (2020), URL <https://link.aps.org/doi/10.1103/PhysRevLett.125.187701>.
- [24] E. A. Laird, F. Kuemmeth, G. A. Steele, K. Grove-Rasmussen, J. Nygård, K. Flensberg, and L. P. Kouwenhoven, *Rev. Mod. Phys.* **87**, 703 (2015), URL <https://link.aps.org/doi/10.1103/RevModPhys.87.703>.
- [25] C. Samanta, D. A. Czaplewski, S. L. De Bonis, C. B. Moller, R. T. Queralt, C. S. Miller, Y. Jin, F. Pistolesi, and A. Bachtold, arXiv preprint, arXiv:2207.02291 (2022).
- [26] A. Bachtold, J. Moser, and M. I. Dykman, arXiv preprint arXiv:2202.01819 (2022).
- [27] R. Lifshitz and M. C. Cross, *Reviews of nonlinear dynamics and complexity* **1** (2008).